Experimental Identification and Analysis of the Dynamics of a PHANTOM® Premium 1.5A Haptic Device

Babak Taati
Department of Electrical and Computer Engineering
Queen's University
Kingston, ON K7L 3N6

Amir M. Tahmasebi
School of Computing
Queen's University
Kingston, ON K7L 3N6

Keyvan Hashtrudi-Zaad
khz@post.queensu.ca
Department of Electrical and Computer Engineering
Queen's University
Kingston, ON K7L 3N6
(Corresponding Author)

Abstract

The dynamics of a PHANTOM® Premium 1.5A haptic device from SensAble Technologies, Inc. is experimentally identified and analyzed for different installations of the device and its accessories, such as the typical upright, upside-down, with gimbal and counter-balance weight, and with force sensor [1]. An earlier formulation of the robot dynamic model is augmented with a friction model, linearly parameterized, and experimentally identified using least squares. The identified dynamics are experimentally evaluated with an inverse dynamics controller and verified by comparing user hand force estimates with the measured values. The contribution of different dynamic terms such as inertial, Coriolis and centrifugal, gravitational, and Coulomb and viscous frictions are demonstrated and discussed. The identified model can be used for a variety of haptic applications, such as hand force estimation, accurate active gravity compensation and counter-balance weight determination for various installation conditions, and model-based control for haptic simulations and teleoperation.

1 Introduction

PHANTOM Premium 1.5A is a desktop haptic device by SensAble Technologies, Inc. that provides force feedback in three degrees-of-freedom (DOF) (Massie & Salisbury, 1994). Although PHANTOM has been widely used in haptic and telerobotic applications (Cavusoglu, Sherman, & Tendick, 2002; Mobasser & Hashtrudi-Zaad, 2008; Tavakoli, Patel, & Moallem, 2004), its functionality is not satisfactory for some high performance applications, partly because its electrical and software subsystems are unknown. Accurate dynamic models of the device are desired for control, simulation, and contact force observation.

There are two main approaches for identifying the device dynamics; (1)*piece-wise*, and (2)*experimental* identification methods. In the piece-wise method, the mechanical properties of various components of a manipulator such as the mass and inertia of linkages, and stiffness of transmission systems are individually measured (Cavusoglu & Feygin, 2001; Cavusoglu,

[1] PHANTOM® is a registered trademark of SensAble Technologies, Inc.

Feygin, & Tendick, 2002). A major challenge for applying this approach is the need for disassembling the robot, which may not be easy or applicable in many cases. Alternatively, Computer Aided Design (CAD) models have been used to provide an estimate of the mechanical properties based on the geometry and material composition. A challenge in applying such a technique is the introduction of inaccuracies stemming from geometric simplifications, ignoring loose or small components, assuming uniform densities, and inaccuracy in robot hardware assembly. While piece-wise methods can identify mechanical properties of each component, they do not consider complex dynamic effects such as joint friction.

In experimental approaches, an implicit or explicit model of the dynamics of a manipulator in its entirety is derived based on a series of measurements. An example of implicit experimental system identification is training a neural network to encapsulate the dynamics of the robot and to avoid explicit estimation of individual parameters (Xing & Pham, 1995; Smith, Mobasser, & Hashtrudi-Zaad, 2006). In explicit methods, which have been used for industrial robots, the manipulator dynamics is formulated in terms of several dynamic parameters to be identified, based on a series of measurements throughout the robot workspace (Atkeson, An, & Hollerbach, 1986; Bona & Curatella, 2005; Khosla & Kanade, 1985; Tafazoli, Lawrence, & Salcudean, 1999; Yoshida, Ikeda, & Mayeda, 1991). It has been shown that the dynamics of manipulators can be linearly parameterized and identified using least squares estimation (Sciavicco & Siciliano, 2001; Astrom & Wittenmark, 1994). In (Mayeda, Osuka, & Kangawa, 1984), a sequential identification method is presented. Similarly, in (Nakamura & Ghodoussi, 1989; Mayeda, Yoshida, & Osuka, 1988), a subset of all robot parameters, are identified such that they include no redundant parameter and thus, prevent the combinatorial explosion of the total number of parameters to be identified as the number of DOF grows. The accuracy of experimental methods depends on the comprehensiveness of the dynamic model, the accuracy of the recorded measurements, and the richness of the robot trajectory.

It has been noted in (Ma & Hollerbach, 1996) that accurate identification of gravitational

parameters for some manipulators is sufficient for many tasks. A rotation command is applied to each joint separately, a sinusoidal curve is fit to the resulting data, and the link mass parameters are estimated statically and separately. The algorithm avoids the need for numerical derivative calculations as required in (Atkeson et al., 1986; Bona & Curatella, 2005; Khosla & Kanade, 1985; Tafazoli et al., 1999; Yoshida et al., 1991). While the approach is accurate and robust, it is not suitable for PHANTOM haptic device, since, the gravity effect is dominated by other dynamic components such as inertia, as it will be shown in Section 4.1. An alternative approach for isolating link dynamics is presented in (Tam, Kubica, & Wang, 2005) in order to simplify the identification process for haptic devices. In the developed technique, joint isolation is achieved by iteratively locking all the joints except one during the identification process; thus, identifying parameters of each joint separately. Determining of the sequence of joints to lock is established by observing the parameters that affect the configuration of each locked joint.

Unlike piece-wise methods, the explicit experimental methods can only identify a subset of parameters that are a combination of the individual properties of various components . However, even though the mass and inertial parameters of each component are not individually identified, the estimated set of parameters are sufficient for many applications, including torque and force estimation and model-based control. The important advantages of experimental over piece-wise methods are in their ability to include friction dynamic effects, and to account for any change in manipulator dynamics due to various configurations or added accessories.

In this work, the dynamic parameter identification of a PHANTOM Premium 1.5A is experimentally investigated for various configurations. The proposed method in this article uses the dynamic structure derived in (Cavusoglu & Feygin, 2001; Cavusoglu, Feygin, & Tendick, 2002). The method avoids some of the assumptions made in (Cavusoglu & Feygin, 2001; Cavusoglu, Feygin, & Tendick, 2002) such as uniformity of link densities and it can be applied to some other models of PHANTOM series devices such as PHANTOM Premium 1.0

and 3.0. The method can easily be applied every time the dynamics of the device is modified. This happens frequently as researchers often use PHANTOM in different configurations (e.g. upside-down) or with different sensors and tools, which changes mass, inertia, and the lengths of different segments of the robot. In such cases, piece-wise methods are time consuming and are often not sufficiently accurate, particularly if the added tools do not have simple geometric shapes.

For evaluating the identified model, an inverse dynamics position controller using the identified model is experimentally shown to be more stable and more responsive than the controller that uses the CAD-based identified dynamic parameters. In addition, hand force estimation including device dynamics proves to be more accurate than the one obtained using only the device geometrical Jacobian, derived in (Cavusoglu & Feygin, 2001). A more in depth analysis of the robot dynamics is also provided for each joint and configuration by looking at the contribution of various torque components in the dynamic model, such as inertial, Coriolis and centrifugal, gravitational, and Coulomb and viscous frictions. The above dynamic dissection can also be utilized for accurate determination of the counter-balancing weights by observing the isolated gravitational term for each joint.

This article is organized as follows: The dynamics equations of the PHANTOM robot, including friction effects, are presented and linearly parameterized in Section 2. The parameters of the dynamic model for various configurations of PHANTOM are experimentally identified and verified in Section 3. The identified dynamic model is used in Section 4 to obtain insight into the system dynamic components, to estimate the counter-balance weights required to compensate for the gravitational effect of the device attachments, to implement an inverse dynamics controller and to provide an estimate of the user hand force. Finally, Section 5 draws conclusions.

2 Dynamic Model

The PHANTOM Premium 1.5A has three degrees of mobility (3 joints) and provides three translational DOF at its end-point. Figure 1 shows the schematics of the device with three motors and the corresponding joint angles, θ_1, θ_2, and θ_3, and a Cartesian frame attached to the end-point of the manipulator.

Figure 1 Here

The dynamics of a robotic manipulator can be formulated as shown in (1):

$$\boldsymbol{\tau} = \mathbf{M}(\boldsymbol{\Theta})\ddot{\boldsymbol{\Theta}} + \mathbf{C}(\boldsymbol{\Theta}, \dot{\boldsymbol{\Theta}})\dot{\boldsymbol{\Theta}} + \mathbf{N}(\boldsymbol{\Theta}) \tag{1}$$

where $\mathbf{M}$, $\mathbf{C}$, and $\mathbf{N}$ represent the inertial matrix, Coriolis and centrifugal matrix, and gravitational vector, respectively, defined in terms of the inertial and kinematic properties of the robot individual components (Sciavicco & Siciliano, 2001). Here, $\boldsymbol{\tau} = [\tau_1 \;\; \tau_2 \;\; \tau_3]^T$ and $\boldsymbol{\Theta} = [\theta_1 \;\; \theta_2 \;\; \theta_3]^T$ are torques vector delivered by the motors and the vector of joint angles derived from the encoders, respectively (Cavusoglu & Feygin, 2001; Cavusoglu, Feygin, & Tendick, 2002).

Using the Euler-Lagrange method, Cavusoglu et al. derived the dynamics structure and equations of motion for PHANTOM 1.5A as given in (2):

$$\begin{bmatrix} \tau_1 \\ \tau_2 \\ \tau_3 \end{bmatrix} = \begin{bmatrix} M_{11} & 0 & 0 \\ 0 & M_{22} & M_{23} \\ 0 & M_{32} & M_{33} \end{bmatrix} \begin{bmatrix} \ddot{\theta}_1 \\ \ddot{\theta}_2 \\ \ddot{\theta}_3 \end{bmatrix} + \begin{bmatrix} C_{11} & C_{12} & C_{13} \\ C_{21} & 0 & C_{23} \\ C_{31} & C_{32} & 0 \end{bmatrix} \begin{bmatrix} \dot{\theta}_1 \\ \dot{\theta}_2 \\ \dot{\theta}_3 \end{bmatrix} + \begin{bmatrix} 0 \\ N_2 \\ N_3 \end{bmatrix} \tag{2}$$

The reader should note that since the electric dynamics of the motors and the voltage amplifier box are assumed to be much faster than the mechanical dynamics of the motors and the linkages, the torque command voltages sent out to the amplifier box are proportional to the motor induced torques. Therefore, the actual motor induced torques reported in this

article, i.e. $\boldsymbol{\tau}$, are found by scaling down the torque command voltages by about a factor of $\alpha = 2.7$. From now on, "torque" refers to the actual motor induced torque.

To identify the device dynamics, (2) is linearly parameterized as:

$$\boldsymbol{\tau} \;=\; \mathbf{Y}(\boldsymbol{\Theta}, \dot{\boldsymbol{\Theta}}, \ddot{\boldsymbol{\Theta}})\boldsymbol{\pi} \tag{3}$$

where $\mathbf{Y}$ is the regressor matrix and $\boldsymbol{\pi}$ is the vector of 8 unknown parameters, defined as in (4) and (5):

$$\mathbf{Y}^T = \begin{bmatrix} \mathbf{Y}_d{}^T \\ -- \\ \mathbf{Y}_g{}^T \end{bmatrix} = \begin{bmatrix} \ddot{\theta}_1 & 0 & 0 \\ \ddot{\theta}_1 c_{2.2} - 2\dot{\theta}_1\dot{\theta}_2 s_2 c_2 - \dot{\theta}_1\dot{\theta}_2 s_{2.2} & \dot{\theta}_1^2 s_{2.2} & 0 \\ \ddot{\theta}_1 c_{2.3} - 2\dot{\theta}_1\dot{\theta}_3 s_3 c_3 - \dot{\theta}_1\dot{\theta}_3 s_{2.3} & 0 & \dot{\theta}_1^2 s_{2.3} \\ \ddot{\theta}_1 c_2 s_3 - \dot{\theta}_1\dot{\theta}_2 s_2 s_3 + \dot{\theta}_1\dot{\theta}_3 c_2 c_3 & -\frac{1}{2}\ddot{\theta}_3 s_{23} + \frac{1}{2}\dot{\theta}_1^2 s_2 s_3 + \frac{1}{2}\dot{\theta}_3^2 c_{23} & -\frac{1}{2}\ddot{\theta}_2 s_{23} - \frac{1}{2}\dot{\theta}_1^2 c_2 c_3 + \frac{1}{2}\dot{\theta}_2^2 c_{23} \\ 0 & \ddot{\theta}_2 & 0 \\ 0 & 0 & \ddot{\theta}_3 \\ ---------- & ---------- & ---------- \\ 0 & c_2 & 0 \\ 0 & 0 & s_3 \end{bmatrix} \tag{4}$$

$$\boldsymbol{\pi}=\begin{bmatrix}\boldsymbol{\pi}_d\\ --\\ \boldsymbol{\pi}_g\end{bmatrix}=\begin{bmatrix}\frac{1}{8}(4I_{ayy}+4I_{azz}+8I_{baseyy}+4I_{beyy}+4I_{bezz}+4I_{cyy}+4I_{czz}\\ +4I_{dfyy}+4I_{dfzz}+L_1^2m_c+L_2^2m_a+4L_3^2m_c+4L_1^2m_a)\\ \frac{1}{8}(4I_{beyy}-4I_{bezz}+4I_{cyy}-4I_{czz}+4L_1^2m_a+L_1^2m_c)\\ \frac{1}{8}(4I_{ayy}-4I_{azz}+4I_{dfyy}-4I_{dfzz}-L_2^2m_a-4L_3^2m_c)\\ L_1(L_2m_a+L_3m_c)\\ \frac{1}{4}(4I_{bexx}+4I_{cxx}+4L_1^2m_a+L_1^2m_c)\\ \frac{1}{4}(4I_{axx}+4I_{dfxx}+L_2^2m_a+4L_3^2m_c)\\ ----------\\ \frac{g}{2}(2L_1m_a+2L_5m_{be}+L_1m_c)\\ \frac{g}{2}(L_2m_a+2L_3m_c-2L_6m_{df})\end{bmatrix} \tag{5}$$

where $\boldsymbol{\pi}_d$ and $\boldsymbol{\pi}_g$ represent dynamic and gravitational parameter vectors, respectively. The inertial and kinematic parameters L_1, L_2, L_3, L_5, L_6, I_{axx}, I_{ayy}, I_{azz}, I_{cxx}, I_{cyy}, I_{czz}, I_{baseyy}, I_{bexx}, I_{beyy}, I_{bezz}, I_{dfxx}, I_{dfyy}, I_{dfzz}, m_a, m_c, m_{be}, and m_{df} are the same as the ones defined in (Cavusoglu, Feygin, & Tendick, 2002) and g is the gravity acceleration. The $\mathbf{Y}$ matrix, given in (4), contains all the terms in (1) that are functions of the robot configuration vector $\boldsymbol{\Theta}$. Here, s_i, c_i, s_{ij}, c_{ij}, $s_{2.i}$, and $c_{2.i}$, $i,j=1,2,3$, represent the shorthand notation for $\sin(\theta_i)$, $\cos(\theta_i)$, $\sin(\theta_i-\theta_j)$, $\cos(\theta_i-\theta_j)$, $\sin(2\theta_i)$, and $\cos(2\theta_i)$, respectively.

The following Coulomb and viscous friction models

$$\tau_{f_i}=\pi_{fc_i}sgn(\dot{\theta}_i)+\pi_{fv_i}\dot{\theta}_i \qquad ,i=1,2,3 \tag{6}$$

or

$$\boldsymbol{\tau}_f=\begin{bmatrix}\tau_{f_1}\\ \tau_{f_2}\\ \tau_{f_3}\end{bmatrix}=\begin{bmatrix}\pi_{fc_1}sgn(\dot{\theta}_1)+\pi_{fv_1}\dot{\theta}_1\\ \pi_{fc_2}sgn(\dot{\theta}_2)+\pi_{fv_2}\dot{\theta}_2\\ \pi_{fc_3}sgn(\dot{\theta}_3)+\pi_{fv_3}\dot{\theta}_3\end{bmatrix}=\mathbf{Y}_f\boldsymbol{\pi}_f \tag{7}$$

are also employed to include the effect of friction, where $sgn(.)$ denotes the signum function, π_{fc_i} and π_{fv_i} represent the Coulomb and viscous friction coefficients for joint "i", respectively, and $\mathbf{Y}_f$ and $\boldsymbol{\pi}_f$ are defined as:

$$\mathbf{Y}_f = \begin{bmatrix} \dot{\theta}_1 & 0 & 0 & sgn(\dot{\theta}_1) & 0 & 0 \\ 0 & \dot{\theta}_2 & 0 & 0 & sgn(\dot{\theta}_2) & 0 \\ 0 & 0 & \dot{\theta}_3 & 0 & 0 & sgn(\dot{\theta}_3) \end{bmatrix} \tag{8}$$

$$\boldsymbol{\pi}_f = [\pi_{fv_1} \quad \pi_{fv_2} \quad \pi_{fv_3} \quad \pi_{fc_1} \quad \pi_{fc_2} \quad \pi_{fc_3}]^T \tag{9}$$

Considering friction effects in the dynamic model, the total $\mathbf{Y}$ and $\boldsymbol{\pi}$ expand to:

$$\boldsymbol{\pi} = \begin{bmatrix} \boldsymbol{\pi}_d \\ -- \\ \boldsymbol{\pi}_g \\ -- \\ \boldsymbol{\pi}_f \end{bmatrix} \tag{10}$$

and

$$\mathbf{Y}_{[3\times 14]} \;=\; [\mathbf{Y}_{d_{[3\times 6]}} \quad \mathbf{Y}_{g_{[3\times 2]}} \quad \mathbf{Y}_{f_{[3\times 6]}}] \tag{11}$$

The linear system of equations in (3) can be solved using the least squares estimation method if several independent data points are available. To collect this data, the robot is moved along a trajectory and its joint angles and motor torques are recorded for a period of time to create $\boldsymbol{\tau}_N$ and $\mathbf{Y_N}$, which are an ensemble of the torque vectors and regression matrices $\boldsymbol{\tau}$ and $\mathbf{Y}$ stacked over for N samples. The least squares solution for $\boldsymbol{\pi}$ is

$$\hat{\boldsymbol{\pi}} = \left[\left(\mathbf{Y_N^T Y_N}\right)^{-1} \mathbf{Y_N^T}\right] \boldsymbol{\tau}_\mathbf{N} \tag{12}$$

where $\hat{\boldsymbol{\pi}}$ is the estimate of the $\boldsymbol{\pi}$ vector, which minimizes the torque error in the sense of mean square, and $\left(\mathbf{Y_N^T Y_N}\right)^{-1}\mathbf{Y_N^T}$ is called the *left pseudo-inverse* of $\mathbf{Y_N}$. The number of measurements should be large enough to avoid ill-conditioning of matrix $\mathbf{Y_N}$ and to assure the existence of the left pseudo-inverse matrix.

As stated earlier, experimental parameter identification cannot identify the property of each dynamic component of the manipulator. Specifically, (5) illustrates that the first 8 elements of the $\boldsymbol{\pi}$ vector are each a combination of several mass, inertial, and length properties for various links of the robot. It should be noted that while the properties of robot joints and components are not individually identified, the set of identified parameters is sufficient for model-based control and hand force estimation.

3 Experiments

In this section, the PHANTOM's dynamic parameters are experimentally estimated and the identified dynamics are discussed and analyzed. The experimental setup, various configurations of the robot, and a filtering technique for avoiding double differentiation for estimating joint acceleration are explained in Section 3.1. The identification of the dynamic parameters for various configurations of the robot, with and without friction considerations, are conducted. An initial verification of the derived dynamics based on torque estimation and torque error analysis are presented in Section 3.2.

3.1 Experimental Setup

The experimental setup consists of a PHANTOM Premium 1.5A, an ATI Industrial Automation Nano-17$^{\text{TM}}$ force/torque sensor and a real-time open-architecture control system developed in-house for full functionality of the robot. The developed open-architecture platform that utilizes PHANTOM amplifier box uses a Quanser Q8$^{\text{TM}}$ data acquisition board and WinCon$^{\text{TM}}$ /RTX$^{\text{TM}}$ real-time control system, which links with MATLAB Real-Time

Workshop^{TM} Toolbox [2]. The sensory information provided by the setup are the three motor angles read by encoders, and the six end-point generalized forces provided by the force sensor in three Cartesian directions. The data collection and control processes run at the rate of $1kHz$.

Joint velocities are calculated from joint angles by using a high-pass filter numerical differentiator. Since these calculations are performed off-line, the filter need not be causal, allowing more accurate estimation of joint velocities (Sciavicco & Siciliano, 2001). Numerical calculation of joint accelerations significantly amplifies noise and is not recommended. Instead, a filtering technique proposed in (Hsu, Bodson, Sastry, & Paden, 1987) is used to eliminate the need for acceleration measurement. To this end, the system total dynamic model (3), (10), and (11) is passed through a strictly stable low-pass filter with a transfer function $L(s) = \frac{\omega}{\omega+s}$, $\omega > 0$ to obtain

$$\boldsymbol{\tau}_L = \mathbf{Y}_L(\boldsymbol{\Theta}, \dot{\boldsymbol{\Theta}})\boldsymbol{\pi} \tag{14}$$

where $\mathbf{Y}_L(\boldsymbol{\Theta}, \dot{\boldsymbol{\Theta}})$ and $\boldsymbol{\tau}_L$ are filtered $\mathbf{Y}$ and $\boldsymbol{\tau}$, respectively. Therefore, $\mathbf{Y}_L$ and $\boldsymbol{\tau}_L$ can be used to find $\hat{\boldsymbol{\pi}}$. Figure 2 illustrates the block diagram of the filtering operation.

Figure 2 Here

The regression matrix $\mathbf{Y}_L$ is only a function of the joint angle and velocity vectors $\boldsymbol{\Theta}$ and $\dot{\boldsymbol{\Theta}}$. This is because the filtered acceleration can be written as a function of joint velocity

[2]Open-architecture solutions for both the older PCI-based models of PHANTOM 1.5A and the newer parallel-port-based models are commercially available (QPEK, 2005). In addition to the above open-architecture solution, the OpenHaptics Toolkit from SensAble Technologies (Itkowitz, Handley, & Zhu, 2005), which can be used for both PCI-based and parallel-port-based models of PHANTOM devices, provides low-level direct access to time-stamped joint angular position and motor torques. The joints' angular velocities can be found from differentiation. The toolkit also allows for closing simple trajectory following PD controllers for conducting experiments and collecting identification datasets.

$$\mathbf{Y}_L{}^T = \begin{bmatrix} \mathbf{Y}_{d_L}{}^T \\ -- \\ \mathbf{Y}_{g_L}{}^T \\ -- \\ \mathbf{Y}_{f_L}{}^T \end{bmatrix} = \begin{bmatrix} \omega(\dot{\theta}_1 - \dot{\theta}_{1_L}) & 0 & 0 \\ \omega[\dot{\theta}_1 c_{2.2} - \{\dot{\theta}_1 c_{2.2}\}_L] & \dot{\theta}_1^2 s_{2.2} & 0 \\ \omega[\dot{\theta}_1 c_{2.3} - \{\dot{\theta}_1 c_{2.3}\}_L] & 0 & \dot{\theta}_1^2 s_{2.3} \\ \omega[\dot{\theta}_1 c_2 s_3 - \{\dot{\theta}_1 c_2 s_3\}_L] & -\frac{1}{2}[\omega\dot{\theta}_3 s_{23} - \{\omega\dot{\theta}_3 s_{23} + \dot{\theta}_2\dot{\theta}_3 c_{23} + \dot{\theta}_1^2 s_2 s_3\}_L] & -\frac{1}{2}\omega\dot{\theta}_2 s_{23} + \{\frac{1}{2}\omega\dot{\theta}_2 s_{23} + \dot{\theta}_2^2 c_{23} - \frac{1}{2}\dot{\theta}_1^2 c_2 c_3 - \frac{1}{2}\dot{\theta}_2\dot{\theta}_3 c_{23}\}_L \\ 0 & \omega(\dot{\theta}_2 - \dot{\theta}_{2_L}) & 0 \\ 0 & 0 & \omega(\dot{\theta}_3 - \dot{\theta}_{3_L}) \\ ---------- & ---------- & ---------- \\ 0 & c_2 & 0 \\ 0 & 0 & s_3 \\ ---------- & ---------- & ---------- \\ \dot{\theta}_{1_L} & 0 & 0 \\ 0 & \dot{\theta}_{2_L} & 0 \\ 0 & 0 & \dot{\theta}_{3_L} \\ \{sgn(\dot{\theta}_1)\}_L & 0 & 0 \\ 0 & \{sgn(\dot{\theta}_2)\}_L & 0 \\ 0 & 0 & \{sgn(\dot{\theta}_3)\}_L \end{bmatrix} \tag{13}$$

and filtered velocity; that is, $\ddot{\theta}_{iL} = \omega(\dot{\theta}_i - \dot{\theta}_{iL})$, $i = 1, 2, 3$. The elements of $\mathbf{Y}_L$ are given in (13), where the subscript "L" signifies that the argument has passed through the low-pass filter $L(s)$. In general, by designing the filter such that its cut-off frequency lies between the system bandwidth and the noise frequency, it is possible to attenuate the degrading effects of measurement noise on the identification performance if the spectrum of the excitation input spans over the entire system bandwidth.

For our identification experiments, an angular position tracking PD controller was implemented. The desired joint trajectories were chosen for high-levels of system excitation required for the convergence of the identified parameters to the true values (Otani, Kakizaki,

& Kogure, 1992; Astrom & Wittenmark, 1994). Towards this end, the desired joint trajectories were constructed from several sinusoids with various frequencies and amplitudes for each joint such that the robot traversed throughout its workspace without any attempt to violate its boundaries. Since for a linear system with "n" unknown parameters, the input can be a linear combination of at least n/2 sinusoids with different phases and frequencies, a sum of 10 sinusoidal signals with frequencies ranging from 0.11 to 5 *rad/s* was chosen as the position command for each link.

As deriving the exact workspace boundaries and joint dependencies was beyond the scope of our work, simple joint angle constraints were imposed on the range of the desired joint angles to make sure that the robot did not violate its workspace and its physical limitations. The amplitudes and phase shifts of the sinusoidal components were chosen to comply with the constraints. The cut-off frequency of the low-pass filter was set to $\omega = 10\ rad/s$ which is higher than the input signal bandwidth and much lower than the noise frequency range. Since the sampling frequency was 1 *kHz*, the chosen sine frequencies were well below the Nyquist rate $500Hz$, such that the elements of the regression matrix $\mathbf{Y}_L$ contained most of their energy below the Nyquist rate.

The robot dynamics are nonlinear and applying a simple PD position controller guarantees neither accurate tracking nor asymptotic stability for free motion. In the experiments, the gains of the PD controller were empirically set to values that would preserve system stability throughout the commanded trajectory. Accurate position tracking was not an issue as long as the robot path did not reach the boundaries of the workspace.

The reader should note that the proposed identification method is an off-line process, which runs with a dataset that has already been collected experimentally. Therefore, either the above-mentioned open-architecture solution or OpenHaptics Toolkit (Itkowitz et al., 2005) can be used to implement a simple position PD controller to enable commanding the robot joints through persistently exciting trajectories and to record the angular position, angular velocity, and joint torques of the manipulator required for the off-line parameter

identification [3].

Figure 3 Here

The dynamic parameters of the PHANTOM device were identified for five common configurations of the robot as described below:

Up-right (UR): The most common configuration of the robot, as illustrated in Figure 3(a).

Gimbal and counter-balance weight (GCW): The gimbal and the counter-balance weight supplied by the manufacturer are mounted on the PHANTOM for three added passive rotational DOFs, as shown in Figure 3(b).

Force sensor (FS): Measured hand force can be used for the design of transparent haptic or telerobotic bilateral controllers (see Figure 3(c)).

Upside-down (USD): This configuration of PHANTOM has especially been used in medical simulators for larger user workspace and enhanced ergonomics.

Upside-down plus gimbal and counter-balance weight (USD+GCW): Figure 3(d) shows the upside-down configuration of the robot with gimbal and counter-balance weight mounted for added passive DOFs and higher force dynamic range. This configuration has been reported in an ultrasound-based training simulator (Tahmasebi, Abolmaesumi, Thompson, & Hashtrudi-Zaad, 2005).

Data acquisition was performed for a duration of over 40 seconds in all experiments. Since the low-pass filter was implemented using a memory unit in the discrete time domain, the first few seconds of the filtered data were discarded to allow for the output of the filter to converge. The first half of the remaining collected data was utilized to identify the dynamic parameters. For cross validation, the estimated parameters were then employed to predict joint torques with the second half of the collected data. Since filtered values of torque and joint velocities were used in the estimation process, the filtered torques were compared with

[3]The proposed identification algorithm, programmed in MATLAB, is available through the corresponding author's website.

their corresponding predicted values.

3.2 Dynamic Parameter Identification and Torque Estimation

In the first experiment that was conducted in the UR configuration, friction parameters were not included and only 8 dynamic parameters, $\boldsymbol{\pi}_d$ and $\boldsymbol{\pi}_g$ in (5) were identified. Figure 4 compares the filtered measured torque ($\boldsymbol{\tau}_L$) with the two estimated filtered torques ($\hat{\boldsymbol{\tau}}_L = \mathbf{Y}_L\hat{\boldsymbol{\pi}}$), one using the identified parameters and the other one using the calculated parameters in (Cavusoglu & Feygin, 2001; Cavusoglu, Feygin, & Tendick, 2002). The large errors between the actual and the estimated filtered torques for joints 1 and 2 were expected and they represent the unaccounted friction effect in the joints and the power transmission system.

Figure 4 Here

Figure 5 Here

Figure 6 Here

Figure 7 Here

To better visualize the effect of friction, the filtered torque prediction errors, $\boldsymbol{\tau}_L - \hat{\boldsymbol{\tau}}_L$, are plotted versus joint velocities in Figure 5. As it can be observed from Figure 5, substantial friction exists in all joints, particularly in joint 1. Therefore, six additional friction parameters were included in the dynamic model. In total, 14 $\boldsymbol{\pi}$ parameters in (11) were identified. Figure 6 illustrates the estimated torques for the UR configuration with the identified parameters after including friction in the model. It can be observed that the estimation errors are substantially less than those without friction consideration and the predicted torques follow the actual values closely. The filtered torque prediction errors are plotted versus joint velocities in Figure 7. The residual error can correspond to other effects such as those unaccounted in the friction model, flexibilities in joints and linkages, measurement and round-off errors, as well as ignored dynamics in sensors and the amplifier. The predicted torques closely follow the actual values in other configurations of the device as well. Figure 8 for

instance, compares the actual filtered torque and the estimated torque in the USD+GCW configuration.

Figure 8 Here

The 14 element parameter vector $\boldsymbol{\pi}$, including the friction coefficients, for all five configurations and the 8 parameters calculated from the piece-wise method in (Cavusoglu, Feygin, & Tendick, 2002) are listed in Table 1. The standard deviations of the estimates are small, in the range of 10^{-3} to 10^{-5}. For the entire workspace of the robot and for all configurations, the estimate of the inertia matrix was confirmed to be positive definite with the minimum eigenvalue of 1.8×10^{-3}. The percent relative root mean square (RMS%) of the filtered torque estimation error (Tafazoli et al., 1999), that is

$$\text{RMS\%} = \sqrt{\frac{\sum_{i=1}^{N}(\hat{\boldsymbol{\tau}}_{Li} - \boldsymbol{\tau}_{Li})^2}{\sum_{i=1}^{N} \boldsymbol{\tau}_{Li}^2}} \times 100 \tag{15}$$

has been calculated for all configurations and listed in Table 2, where N is the total number of samples. The following observations can be made from studying Tables 1 and 2, and Figures 8 and 9:

1. The corresponding $\hat{\boldsymbol{\pi}}_d$ parameters from (Cavusoglu, Feygin, & Tendick, 2002) and the UR column have the same signs and are relatively close. This validates the assumptions made in the piece-wise method in (Cavusoglu, Feygin, & Tendick, 2002). The largest difference is observed in $\hat{\boldsymbol{\pi}}_{d1}$, perhaps because $\boldsymbol{\pi}_{d1}$ includes nearly all the system's mass and inertia parameters. Therefore, the errors in the piece-wise estimation of these dynamic parameters accumulate, resulting in such a difference.

2. Comparing π_{d1} to π_{d6} in UR and GCW columns shows that adding gimbal and counterbalance weight adds substantially to the device's inertia.

3. Comparing π_{d1} to π_{g8} for UR and USD configurations shows that changing the PHANTOM configuration to USD does not change the dynamic parameters except for the sign of the gravitational parameters π_{g7} and π_{g8}. This confirms the fact that in UR

$\hat{\pi}$ $\times 1000$	piece-wise	UR	GCW	FS	USD	USD+ GCW
$\hat{\pi}_{d1}$	2.78	1.42	3.40	1.02	1.20	3.04
$\hat{\pi}_{d2}$	1.09	1.35	4.43	2.16	1.61	3.29
$\hat{\pi}_{d3}$	-0.40	-0.40	-1.17	-0.76	-0.51	-0.73
$\hat{\pi}_{d4}$	0.91	0.69	9.23	3.00	0.65	9.19
$\hat{\pi}_{d5}$	2.41	2.08	7.54	3.47	2.85	6.37
$\hat{\pi}_{d6}$	0.91	0.95	3.55	1.13	1.28	3.15
$\hat{\pi}_{g7}$	-16.30	-19.23	26.92	46.84	21.24	-16.59
$\hat{\pi}_{g8}$	-73.80	-109.96	46.52	-69.08	108.75	-112.45
$\hat{\pi}_{f9}$	-	-2.08	-2.71	-0.91	-1.35	-0.10
$\hat{\pi}_{f10}$	-	-1.28	0.10	-0.32	-0.14	0.54
$\hat{\pi}_{f11}$	-	-0.18	1.13	0.43	0.91	0.73
$\hat{\pi}_{f12}$	-	25.89	26.22	27.06	26.08	24.35
$\hat{\pi}_{f13}$	-	9.19	8.35	9.34	8.24	7.28
$\hat{\pi}_{f14}$	-	9.08	9.04	10.00	8.09	8.71

Table 1: Estimated π parameters of different configurations: GCW: Gimbal and Counter-balance Weight, FS: Force Sensor, USD: Upside-Down, USD+GCW: Upside-Down + Gimbal and Counter-balance Weight.

and USD configurations the arm moves in opposite directions when the motors are not activated.

4. By adding gimbal and counter-balance weight to the USD configuration, π_{g7} and π_{g8} change their signs, and thus, the added weight overcompensates for gravity.

5. The gravitational parameters π_{g7} and π_{g8}, change from -19.23 and $-109,96$ to 46.84 and -69.08 for the FS configuration. The change of sign in π_{g7} and the reduction in π_{g8} imply that force sensor at the tip acts as a counter-balance weight for the UR configuration. For bulkier force sensors, the gravitational effect needs to be compensated by a counter-balance weight on the motors.

RMS%	UR	GCW	FS	USD	USD+GCW
τ_1	12.4	19.0	17.0	13.7	19.2
τ_2	10.7	28.2	10.4	9.0	11.3
τ_3	3.2	14.6	13.0	4.5	17.0

Table 2: RMS% values of the actual and estimated torque errors for different configurations; GCW: Gimbal and Counter-balance Weight, FS: Force Sensor, USD: Upside-Down, USD+GCW: Upside-Down + Gimbal and Counter-balance Weight.

6. Comparing π_{f9} to π_{f14} for all configurations shows that joint one has the most significant Coulomb and viscous friction among all three, followed by joint three and then two. Also, the effect of Coulomb friction is consistently higher than the effect of viscous friction for such ranges of speed. The absolute values of π_{fc_i}/π_{fv_i}, $i = 1, 2, 3$, according to (6), provide an upper bound on joint velocities, up to which the Coulomb friction remains larger than the viscous friction. For instance, for the UR configuration, the angular velocity limits for joints 1, 2, and 3 are 710 deg/s, 412 deg/s, and $2,841$ deg/s, respectively. In order to grasp a better view on the effect of each friction component, Coulomb and viscous friction terms are illustrated separately in Figure 9 for the UR configuration. As illustrated, Coulomb friction is the dominant friction term in all three joints.

7. Considering the RMS% values in Table 2, it is clear that the GCW and USD+GCW configurations have the most significant errors. This can be due to the movement of the gimbal since it is difficult to rigidly fix the gimbal to the robot arm, while the arm is moving. Any small movement of the gimbal can noticeably change the dynamics of the robot.

Figure 9 Here

4 Applications of the Identified Dynamics

In this section, the identified dynamics of the PHANTOM are used to obtain *i)* a general understanding of the major contributors to each joint dynamics, *ii)* an estimate of the counter-balance weight needed for each robot configuration and added tool attachment, *iii)* a more precise and robust inverse dynamics control, and iv) an online estimate of contact forces at the tip position of the robot.

4.1 Dynamic Dissection

Figure 10 Here

In order to further analyze system dynamics, the estimated $\boldsymbol{\pi}$ parameters are employed to calculate the joint torques and the contributions of inertia, Coriolis and centrifugal, gravity and friction torque terms for each configuration for random free motion operation with a maximum velocity 3.5 rad/s = 200.6 deg/s. Figure 10 shows the contribution of each dynamic term in each joint torque for the UR configuration, whereas Figure 11 demonstrates the contribution of each term in the joint 3 torque for all configurations. The following observations can be made:

1. Joint 1: For all configurations, the most significant contribution comes from friction and then Coriolis and centrifugal terms.

2. Joint 2: The main contribution comes from the inertial term and then Coriolis and centrifugal terms, especially when the gimbal and counter-balance weight are added (not shown in the figures).

3. Joint 3: In general, the contribution of gravity to torque is the most significant in joint 3 compared to the other two joints. Adding extra mass such as a force sensor to the UR configuration cuts down the effect of gravity by half, whereas adding a gimbal and counter-balance weight almost practically nulls the effect of gravity at the expense of a significant increase in inertial torque.

Figure 11 Here

4.2 Counter-balance Weight Estimation

The identified dynamics can also be utilized to obtain a relatively accurate initial estimate of the counter-balance weight required for any configuration and added accessory.

The gravitational parameters π_{g7} and π_{g8} in (5) are determined by the mass and length properties of various links of the robot as described in detail in (Cavusoglu & Feygin, 2001; Cavusoglu, Feygin, & Tendick, 2002). Adding a lumped mass m_{ep} at the end-point (EP), such as a gimbal or a force sensor, and mounting predesigned counter-balance weights m_{cb2} and m_{cb3} on motors 2 and 3 will result in the following changes to the gravitational parameters:

$$\pi'_{g7} = \pi_{g7} - g m_{cb2} L_{cb} + g m_{ep} L_1 \quad (16)$$

$$\pi'_{g8} = \pi_{g8} - g m_{cb3} L_{cb} + g m_{ep} L_{ep} \quad (17)$$

where $L_{cb} \geq 0$ is the distance between the center of gravity of the counter-balance weight and the horizontal axis of the vertical capstan, and L_{ep} is the distance between the center of gravity of the EP attachment and the distal end of the last link, as shown in Figure 12. It is assumed that the center of gravity of the attachment is along the last link. To investigate Equations (16)-(17), the gravitational parameters for the USD+GCW configuration are calculated from their corresponding parameters from the UR configuration column of Table 1, i.e. $\pi_{g7} = -0.01923$ and $\pi_{g8} = -0.10996$. For the gimbal with approximate weight $m_{ep} = 0.09\ Kg$, the manufacturer has provided a counter-balance weight $m_{cb2} = 0.216\ Kg$. Considering $L_{cb} \approx 0.075\ m$, $L_{ep} \approx 0.195\ m$, $L_1 = 0.216\ m$ and $g = 9.81\ m/s^2$, and using (16)-(17), the gravitational parameters for the GCW configuration are calculated as $\pi'_{g7} = 0.0223$ and $\pi'_{g8} = 0.0622$, which are a close match to the estimated parameters 0.0269 and 0.0465 from the fourth column of Table 1.

Figure 12 Here

From (17), it is clear that the provided counter-balance weight for motor 2 cannot have any effect on π_{g8}. To compensate for this shortcoming, a second counter-balance weight (m_{cb3}) needs to be mounted on motor 3. The mass of the counter-balance weights that cancels the effect of gimbal on both gravitational parameters such that $\pi'_{g7} = \pi'_{g8} = 0$ can be calculated from:

$$(m_{cb2})_{net} = \frac{\pi_{g7} + g m_{ep} L_1}{g L_{cb}} \tag{18}$$

$$(m_{cb3})_{net} = \frac{\pi_{g8} + g m_{ep} L_{ep}}{g L_{cb}} \tag{19}$$

If the mass of the EP tool or accessory is substantial, the mass of the counter-balance weights become proportional to the mass of the tool according to $m_{cb2} \approx (L_1/L_{cb}) m_{ep}$ and $m_{cb2} \approx (L_{ep}/L_{cb}) m_{ep}$. From (18)-(19), the recommended counter-balance weights for motors 2 and 3 are $(m_{cb2})_{net} = 0.248\ Kg$ and $(m_{cb3})_{net} = 0.091\ Kg$, respectively. It has been noticed that the calculated weights are sensitive to the center of gravity distances L_{ep} and L_{cb}; however, the calculated values provide an initial estimate, which can be fine tuned for any setup and application.

4.3 Inverse Dynamics Control

The identified dynamics of the PHANTOM can be employed to implement inverse dynamics control for haptic or telerobotic bilateral controllers that are designed based on such a control strategy or require linear dynamics for master stability or performance analysis. As a slave, a PHANTOM robot controlled with inverse dynamics can provide more accurate position tracking. Finally, the inverse dynamics experiments in this section also provide a qualitative verification of the proposed parameter estimation technique (Bona & Curatella, 2005).

Figure 13 illustrates a block diagram of a position controlled PHANTOM robot, in which

the control system consists of an inverse dynamics inner control loop and a PD outer control loop (Sciavicco & Siciliano, 2001). The inverse dynamics, which is computed online using the estimated dynamic parameters, tries to ideally cancel the nonlinear dynamic effects and to decouple the resulting linear dynamics. Here **F** represents the friction terms.

Figure 13 Here

If the nonlinearities are fully compensated, adjusting the gains of the PD controller can place the poles of the system for each of the decoupled joints at any desired location as long as the motors are not saturated. In practice, since nonlinear compensation is not perfect, there could be issues with responsiveness and stability of the overall system. In order to empirically analyze the accuracy of the estimated parameters from the piece-wise and the proposed experimental methods, an inverse dynamics + PD controller was implemented in various control parameter settings and for various configurations of the robot. Tracking error of the overall system with low gains and its stability with high gains signify the responsiveness and robustness of the controller and show how well the nonlinearities of the robot dynamics are canceled, which in turn indicate how accurate the dynamic parameters are estimated.

Figure 14 Here

In the experiments the proportional gain was varied from 100 to 1200, and the derivative gain was adjusted to maintain a critically damped or slightly under or over damped ($0.7 \leq \zeta \leq 1.2$) closed-loop decoupled joint dynamics. Since full cancellation of friction could lead to instability, the linearizing feedback loop was tried with 50% friction compensation. The experiments showed that the identified parameters were able to effectively cancel nonlinearities and the performance of the controller was often satisfactory and close to the ideal system, i.e. double integrator stabilized with a PD controller. The following observations were made based on the experimental results:

Figure 15 Here

Figure 16 Here

1. In the UR configuration with light to medium proportional gains ($100 \leq K_P \leq 800$),

the identified parameters and those calculated based on the piece-wise method (Cavusoglu, Feygin, & Tendick, 2002) lead to close set-point tracking with position control, especially for joints 1 and 2. The largest tracking error was observed in joint 3. This indicates that the nonlinearities in this joint were not compensated as well as those in the other two joints. Figure 14 illustrates the position tracking results for joint 3 when K_P and K_D are set to 625 and 35, respectively. The desired input position command is a square pulse with a period of four seconds, while the other two joints are commanded to remain at a constant position. As seen, the performance of the controller with experimentally identified parameters demonstrated lower steady state error (20% compared to 25% error) and lower overshoot.

2. The tracking error was smaller for larger proportional gains since tighter PD control can diminish the nonlinear effects as long as the system does not become unstable. However, increasing the gains to tighter values eventually made the controller unstable. The controller with parameters from piece-wise method (Cavusoglu, Feygin, & Tendick, 2002) became unstable with smaller values of K_P than the experimentally estimated parameters. In other words, the estimated parameters provided stability for a larger range of PD gains. Figure 15 illustrates the joint 3 angle, when K_P and K_D are set to 1200 and 80, respectively.

3. For other configurations, parameters calculated based on the piece-wise method (Cavusoglu, Feygin, & Tendick, 2002) lead to unsatisfactory position tracking with small to medium PD gains, whereas the experimentally identified parameters provided more acceptable tracking even with low proportional gains. Figure 16 illustrates the joint 3 angle for the USD+GCW configuration, when K_P and K_D are set to 100 and 14, respectively.

Overall, the results from the experiments with an inverse dynamics controller illustrated that the identified parameters provided more responsive and more stable position control in comparison to the parameters from the piece-wise method.

4.4 Contact Force Estimation

Haptic interfaces aim to produce a sense of contact between a human and virtual objects by displaying bi-directional forces. To design transparent haptic or telerobotic controllers, high bandwidth contact forces need to be measured or estimated. Using an accurate estimate of PHANTOM's dynamics and kinematic parameters, the external force at the EP, i.e. F_{ext}, can be estimated according to

$$\hat{\mathbf{F}}_{ext} = (\mathbf{J}_p)^{-T}(\boldsymbol{\tau} - \mathbf{Y}\hat{\boldsymbol{\pi}}) \tag{20}$$

where $\mathbf{J}_p$, the translational Jacobian in the EP frame (see Figure 1) relating joint angles to the EP position, is found according to (Cavusoglu & Feygin, 2001; Cavusoglu, Feygin, & Tendick, 2002)

$$\mathbf{J_P} = \begin{bmatrix} l_1c_2 + l_2s_3 & 0 & 0 \\ 0 & l_1c_{23} & 0 \\ 0 & -l_1s_{23} & l_2 \end{bmatrix} \tag{21}$$

Note that in (20) the effect of external torque is neglected since PHANTOM is a point based device with 3-DOF active force feedback; thus, it cannot apply any resistive torque about any axis. The estimated forces are validated by comparing the estimated hand forces with the output of an ATI Nano-17$^{\text{TM}}$ force sensor, mounted at the EP of the device, as shown in Figure 3(c). For consistency with the filtered torque values, the measured forces provided by the force sensor are passed through the low-pass filter of (2) as well.

Figure 17 Here

Figure 17 compares the actual force in the y-direction to the estimated forces obtained from (20) without using the dynamic model (i.e. $\hat{\mathbf{F}}_{ext}(\mathbf{J}_p)^{-T}\boldsymbol{\tau}$). As can be seen in the dynamic condition, especially when the direction of motion changes, force estimation with dynamic model produces slightly better results. Some of the factors that contribute to the observed error in the estimated force are the same as the ones discussed in Section 3.2.

Another possible source of error is the fact that the force sensor frame needs to be registered with the EP frame. In the experiments, the sensor was mounted such that the two frames were visually aligned and the elementary transformation for converting the measurements from the force sensor frame to the EP frame was experimentally derived using least squares.

5 Conclusions

The dynamics of a SensAble Technologies PHANTOM Premium 1.5A are experimentally identified. The advantages of the applied experimental method over the previously developed piece-wise techniques are accuracy, partly due to the inclusion of friction in the dynamics model, ease of use for handling alterations to the device dynamics, and applicability to other models of the PHANTOM. The haptic device dynamics for different configurations were also identified, validated, and analyzed. The parameter estimates produced an inertia matrix that was confirmed to be positive-definite within the device workspace. The identified model also demonstrated noticeable Coulomb friction, especially in joint 1.

The identified dynamics were used to compute the contribution of various dynamic terms in each joint for different configurations. It was noticed that two counter-balance weights are required to cancel the gravitational effect of an end-point tool or accessories such as the gimbal. In addition, the required weights on motors 2 and 3 to cancel the effect of gimbal were calculated. Experiments with model-based position control showed that the identified dynamics provided more robust and more responsive position control than earlier piece-wise (CAD-based) estimations of the robot inertial parameters. Finally, the identified dynamics were utilized to obtain a more accurate estimate of external hand (contact) force.

Acknowledgments

This work was supported in part by Natural Sciences and Engineering Research Council of Canada (NSERC). The authors wish to thank Dr. Farid Mobasser for the development

of the real-time open-architecture control system for PHANTOM and for his help with the experimental setup.

References

Astrom, K. J., & Wittenmark, B. (1994). Adaptive control. *MA: Addison-Wesley Longman.*

Atkeson, C. G., An, C. H., & Hollerbach, J. M. (1986). Estimation of inertial parameters of manipulator links and loads. *International Journal of Robotics Research*, *5*(3), 101-119.

Bona, B., & Curatella, A. (2005). Identification of industrial robot parameters for advanced model-based controllers design. *Proceedings of the International Conference on Robotics and Automation*, 1681- 1686.

Cavusoglu, M. C., & Feygin, D. (2001). Kinematics and dynamics of phantom^{TM} model 1.5 haptic interface. *University of California at Berkeley, Electronic Research Laboratory Memo M01/15.*

Cavusoglu, M. C., Feygin, D., & Tendick, F. (2002). A critical study of the mechanical and electrical properties of the phantom haptic interface and improvements for high performance control. *PRESENCE: Teleoperators and Virtual Environments*, *11*(6), 555-568.

Cavusoglu, M. C., Sherman, A., & Tendick, F. (2002). Design of bilateral teleoperation controllers for haptic exploration and telemanipulation of soft environments. *IEEE Transactions on Robotics and Automation*, *18*(4), 641-647.

Hsu, P., Bodson, P. M., Sastry, S., & Paden, B. (1987). Adaptive identification and control of manipulators without using joint accelerations. *Proceedings of the International Conference on Robotics and Automation*, 1210-1215.

Itkowitz, B., Handley, J., & Zhu, W. (2005). The openhaptics toolkit: a library for adding 3d touch navigation and haptics to graphics applications. *Proceedings of the Eurohaptics Conference and Symposium on Haptic Interfaces for Virtual Environment and Teleoperator Systems*, 590-591.

Khosla, P. K., & Kanade, T. (1985). Parameter identification of robot dynamics. *Proceedings of the IEEE Conference on Decision and Control*, 1754-1760.

Ma, D., & Hollerbach, J. M. (1996). Identifying mass parameters for gravity compensation and automatic torque sensor calibration. *Proceedings of the International Conference on Robotics and Automation*, 661-666.

Massie, T. H., & Salisbury, J. K. (1994). The phantom haptic interface: A device for probing virtual objects. *Proceedings of the ASME Winter Annual Meeting, Symposium on Haptic Interfaces for Virtual Environments and Teleoperator Systems*, 295302.

Mayeda, H., Osuka, K., & Kangawa, A. (1984). A new identification method for serial manipulator arms. *Proceedings of the 9th International Federation of Automatic Control (IFAC) World Congress*, 2429-2434.

Mayeda, H., Yoshida, K., & Osuka, K. (1988). Base parameter of manipulator dynamic models. *Proceedings of the International Conference on Robotics and Automation*, 312-321.

Mobasser, F., & Hashtrudi-Zaad, K. (2008). Transparent rate mode bilateral teleoperation control. *International Journal of Robotics Research*, *27*(1), 57-72.

Nakamura, Y., & Ghodoussi, M. (1989). Base parameter analysis of open and closed link mechanism using covariance matrix of nonlinearity. *Proceedings of the International Conference on Robotics and Automation*, 294-302.

Otani, K., Kakizaki, T., & Kogure, K. (1992). Dynamic parameter identification of an industrial robot and its application to trajectory controls. *Proceedings of the IEEE/RSJ International Conference on Intelligent Robots and Systems*, 990-997.

QPEK. (2005). Quanser phantom expansion kit. *http://www.quanser.com [access date: 27-01-2007].*

Sciavicco, L., & Siciliano, B. (2001). Modelling and control of robot manipulators, 2nd ed. *London, UK: Springer-Verlag Advanced Textbooks in Control and Signal Processing Series.*

Smith, A., Mobasser, F., & Hashtrudi-Zaad, K. (2006). Neural network based contact force observers for haptic applications. *IEEE Transactions on Robotics and Automation*, *22*(6), 1163-1175.

Tafazoli, S., Lawrence, P. D., & Salcudean, S. E. (1999). Identification of inertial and friction parameters for excavator arms. *IEEE Transactions on Robotics and Automation*, *15*(5), 966-971.

Tahmasebi, A. M., Abolmaesumi, P., Thompson, D., & Hashtrudi-Zaad, K. (2005). Software structure design for a haptic-based medical examination system. *Proceedings of the IEEE International Workshop on Haptic Audio Visual Environments and their Applications*, 89-94.

Tam, S., Kubica, E., & Wang, D. (2005). A system identification technique for haptic devices. *Proceedings of the IEEE Conference on Control Applications*, 1240-1245.

Tavakoli, M., Patel, R. V., & Moallem, M. (2004). Design issues in a haptics-based master-slave system for minimally invasive surgery. *Proceedings of the International Conference on Robotics and Automation*, 371-376.

Xing, L., & Pham, D. T. (1995). Neural networks for identification, prediction and control. *NY: Springer-Verlag.*

Yoshida, K., Ikeda, N., & Mayeda, H. (1991). Experimental identification methods for an industrial robot manipulator. *Proceedings of the IEEE/RSJ International Conference on Intelligent Robots and Systems*, 546-560.

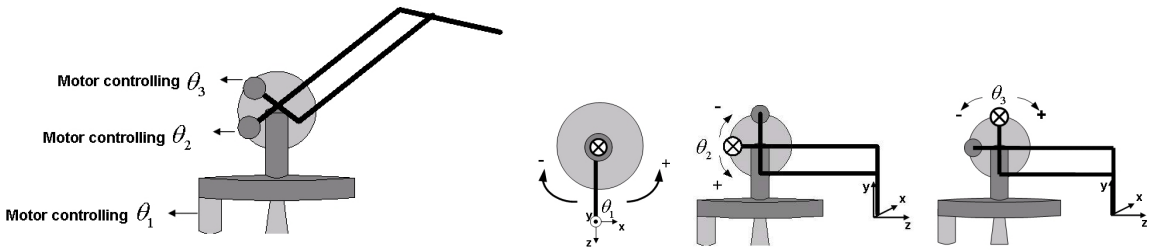
Motor controlling θ_3
Motor controlling θ_2
Motor controlling θ_1
-
+
θ_1
y
x
z
θ_2
-
+
y
x
z
θ_3
-
+
y
x
z

Figure 1:

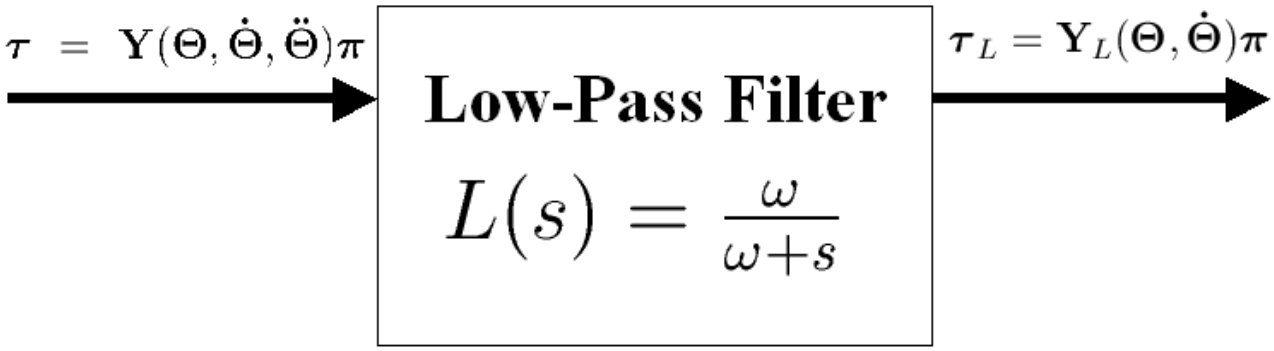
$\tau = \mathbf{Y}(\Theta, \dot{\Theta}, \ddot{\Theta})\pi$
Low-Pass Filter
$L(s) = \frac{\omega}{\omega + s}$
$\tau_L = \mathbf{Y}_L(\Theta, \dot{\Theta})\pi$

Figure 2:

Figure 3:

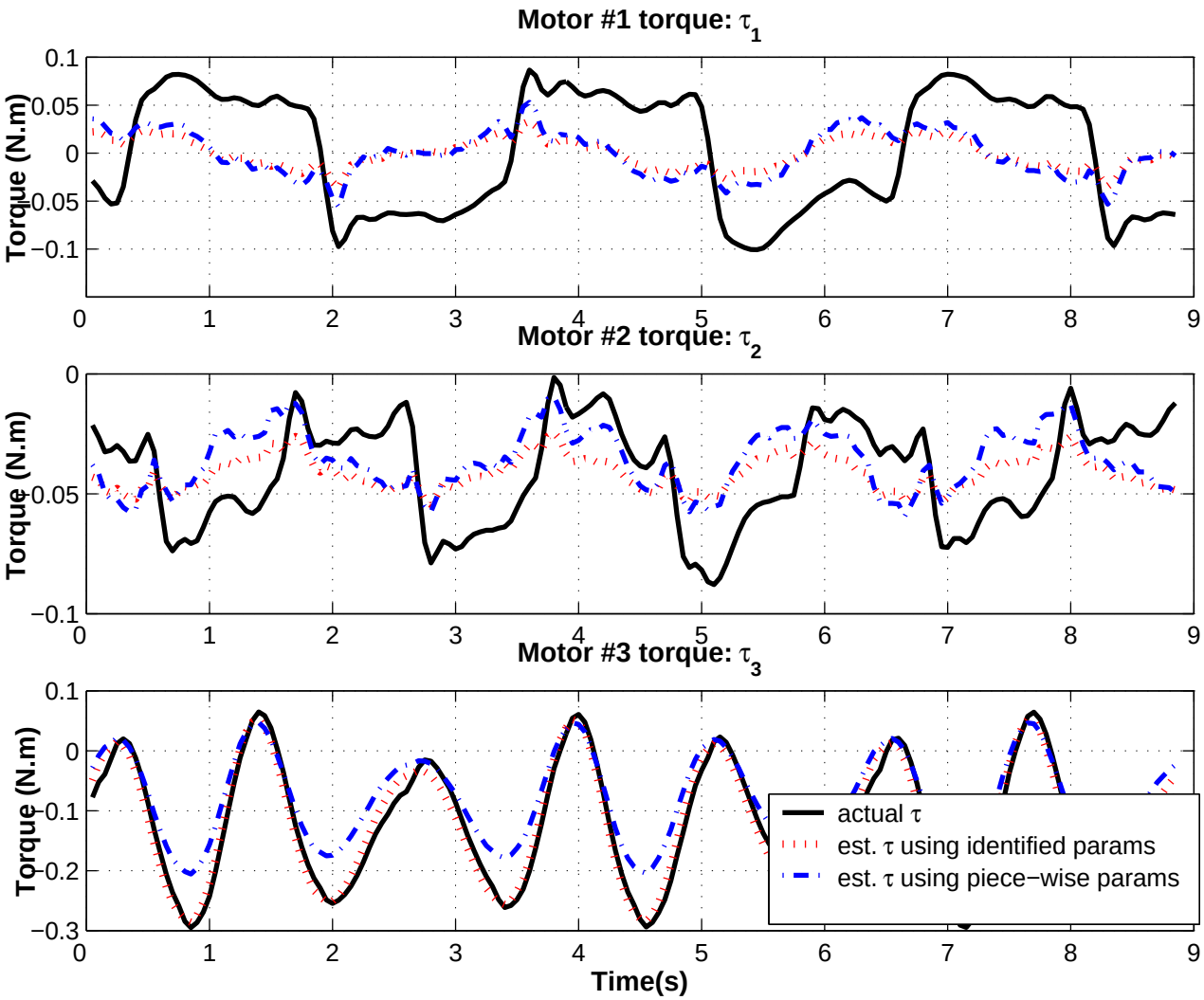
Motor #1 torque: τ1
Torque (N.m)
0.1
0.05
0
−0.05
−0.1
0
1
2
3
4
5
6
7
8
9
Motor #2 torque: τ2
Torque (N.m)
0
−0.05
−0.1
Motor #3 torque: τ3
Torque (N.m)
0.1
0
−0.1
−0.2
−0.3
Time(s)
actual τ
est. τ using identified params
est. τ using piece−wise params

Figure 4:

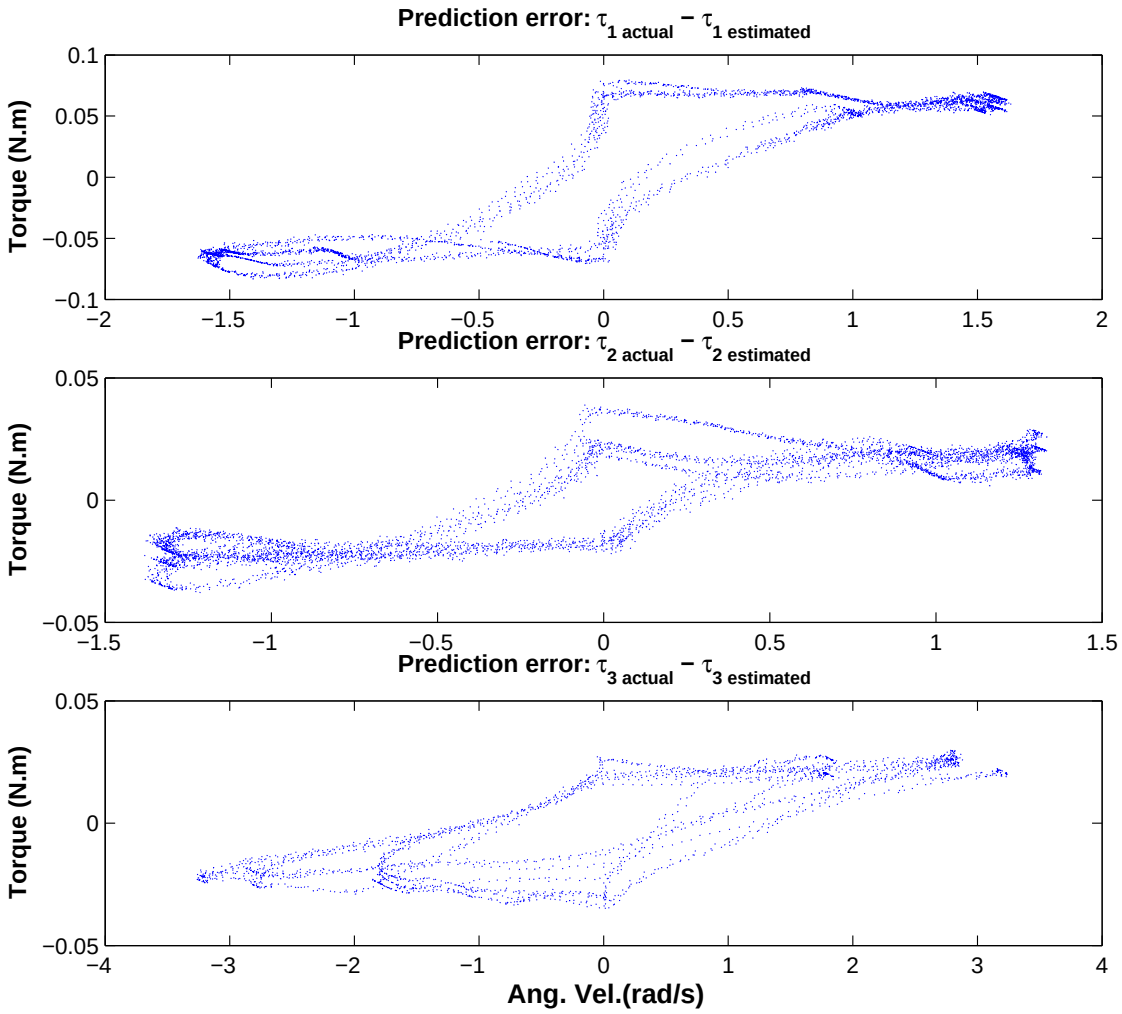
Prediction error: τ1 actual − τ1 estimated
Torque (N.m)
0.1
0.05
0
−0.05
−0.1
−2
−1.5
−1
−0.5
0
0.5
1
1.5
2
Prediction error: τ2 actual − τ2 estimated
Torque (N.m)
0.05
0
−0.05
−1.5
−1
−0.5
0
0.5
1
1.5
Prediction error: τ3 actual − τ3 estimated
Torque (N.m)
0.05
0
−0.05
−4
−3
−2
−1
0
1
2
3
4
Ang. Vel.(rad/s)

Figure 5:

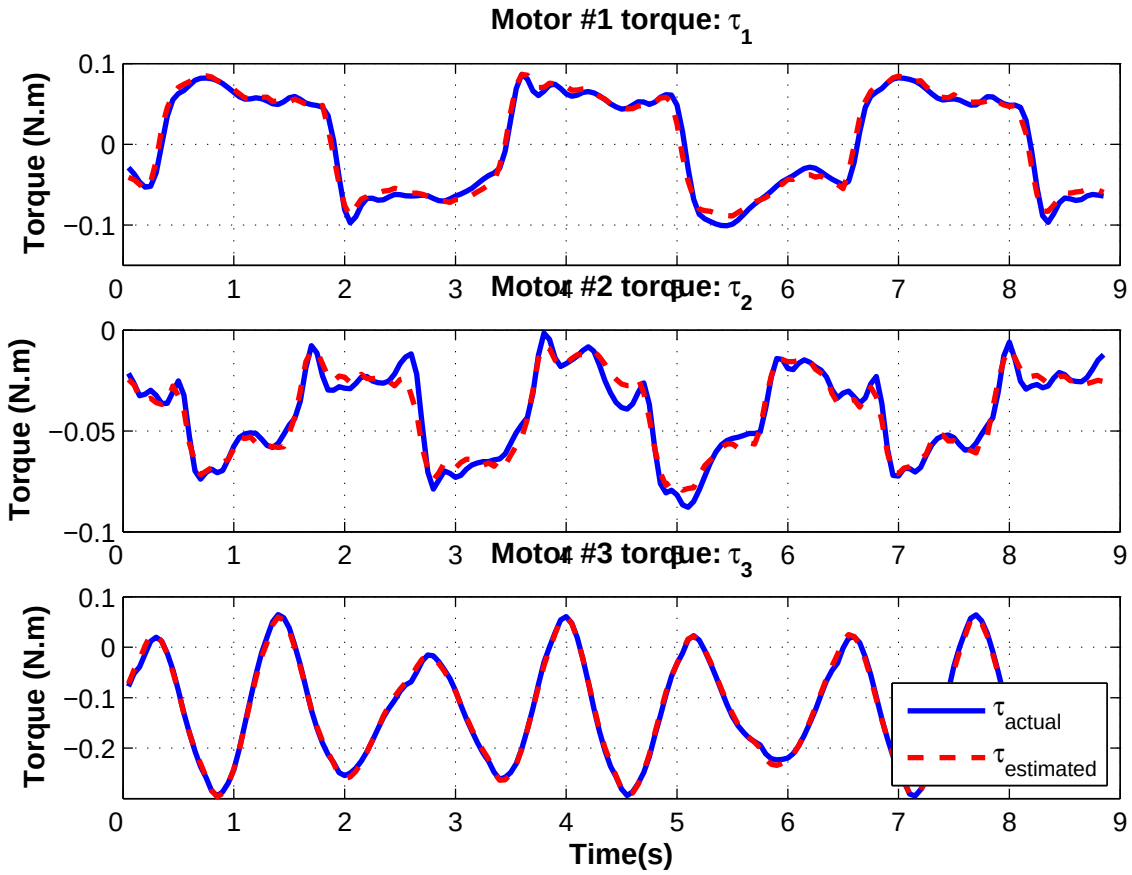
Motor #1 torque: τ_1
Torque (N.m)
0.1
0
−0.1
0
1
2
3
4
5
6
7
8
9
Motor #2 torque: τ_2
Torque (N.m)
0
−0.05
−0.1
Motor #3 torque: τ_3
Torque (N.m)
0.1
0
−0.1
−0.2
τ_{actual}
$\tau_{estimated}$
Time(s)

Figure 6:

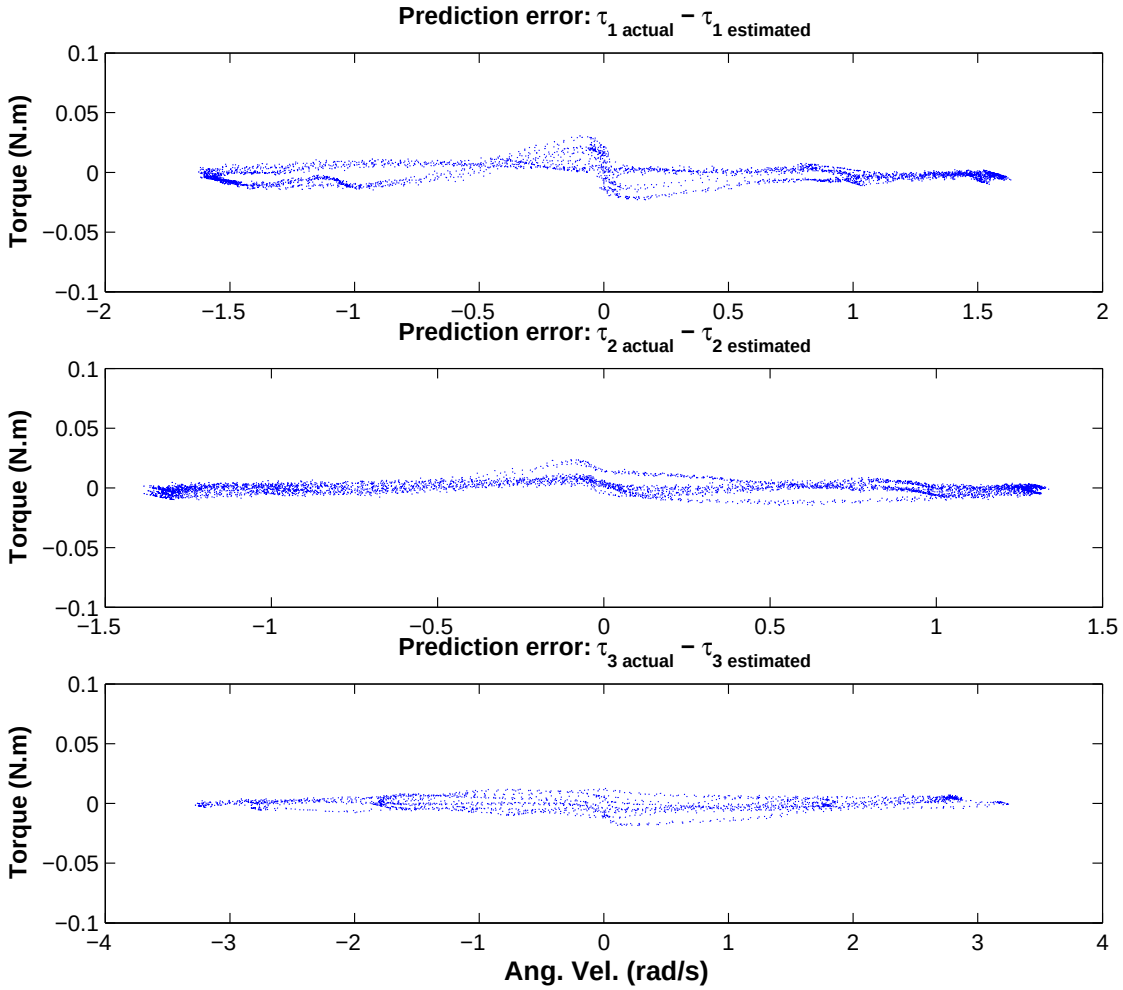
Prediction error: τ1 actual − τ1 estimated
Torque (N.m)
0.1
0.05
0
−0.05
−0.1
−2
−1.5
−1
−0.5
0
0.5
1
1.5
2
Prediction error: τ2 actual − τ2 estimated
Torque (N.m)
0.1
0.05
0
−0.05
−0.1
−1.5
−1
−0.5
0
0.5
1
1.5
Prediction error: τ3 actual − τ3 estimated
Torque (N.m)
0.1
0.05
0
−0.05
−0.1
−4
−3
−2
−1
0
1
2
3
4
Ang. Vel. (rad/s)

Figure 7:

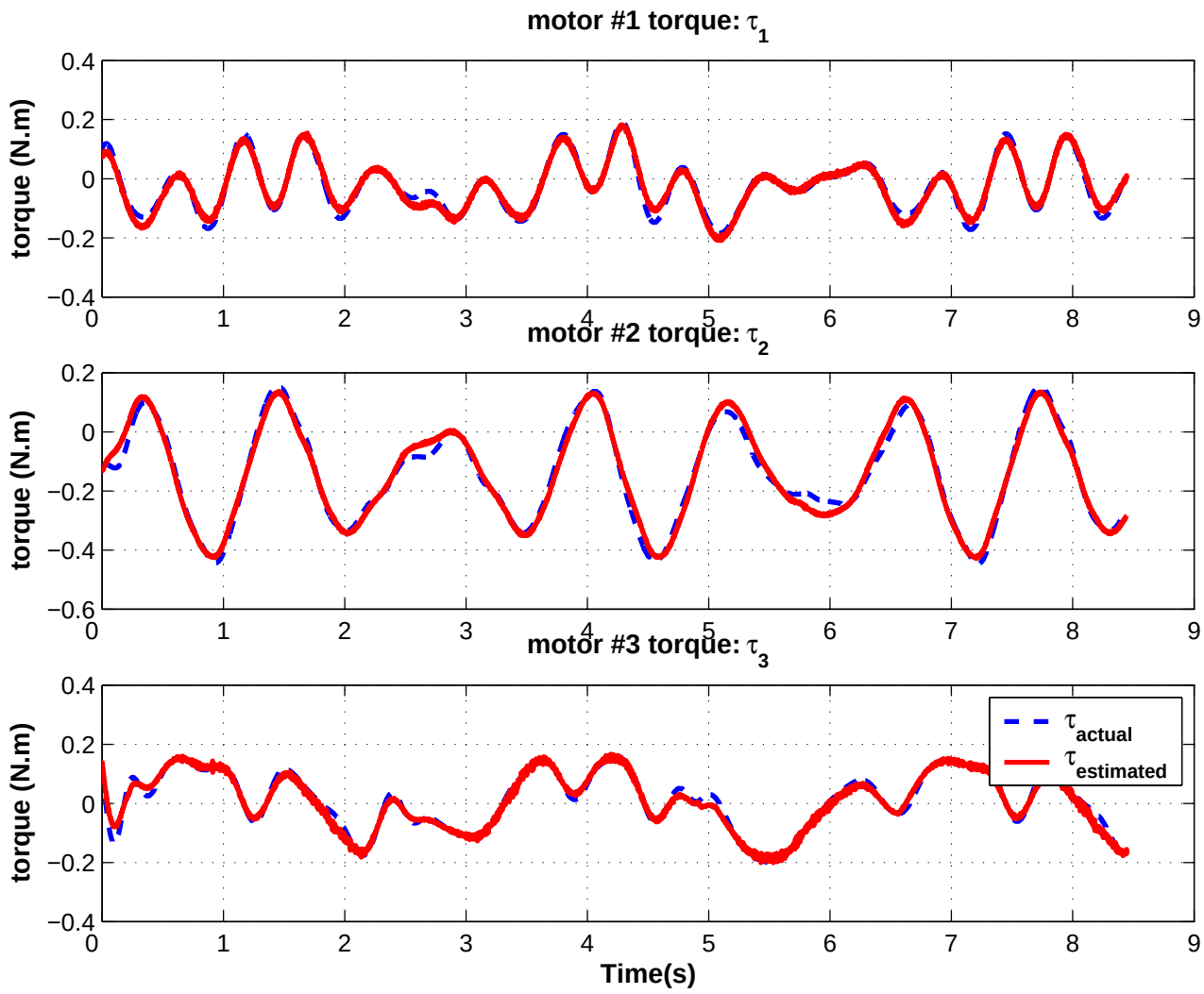
motor #1 torque: τ_1
torque (N.m)
motor #2 torque: τ_2
torque (N.m)
motor #3 torque: τ_3
torque (N.m)
Time(s)
τ_{actual}
$\tau_{estimated}$

Figure 8:

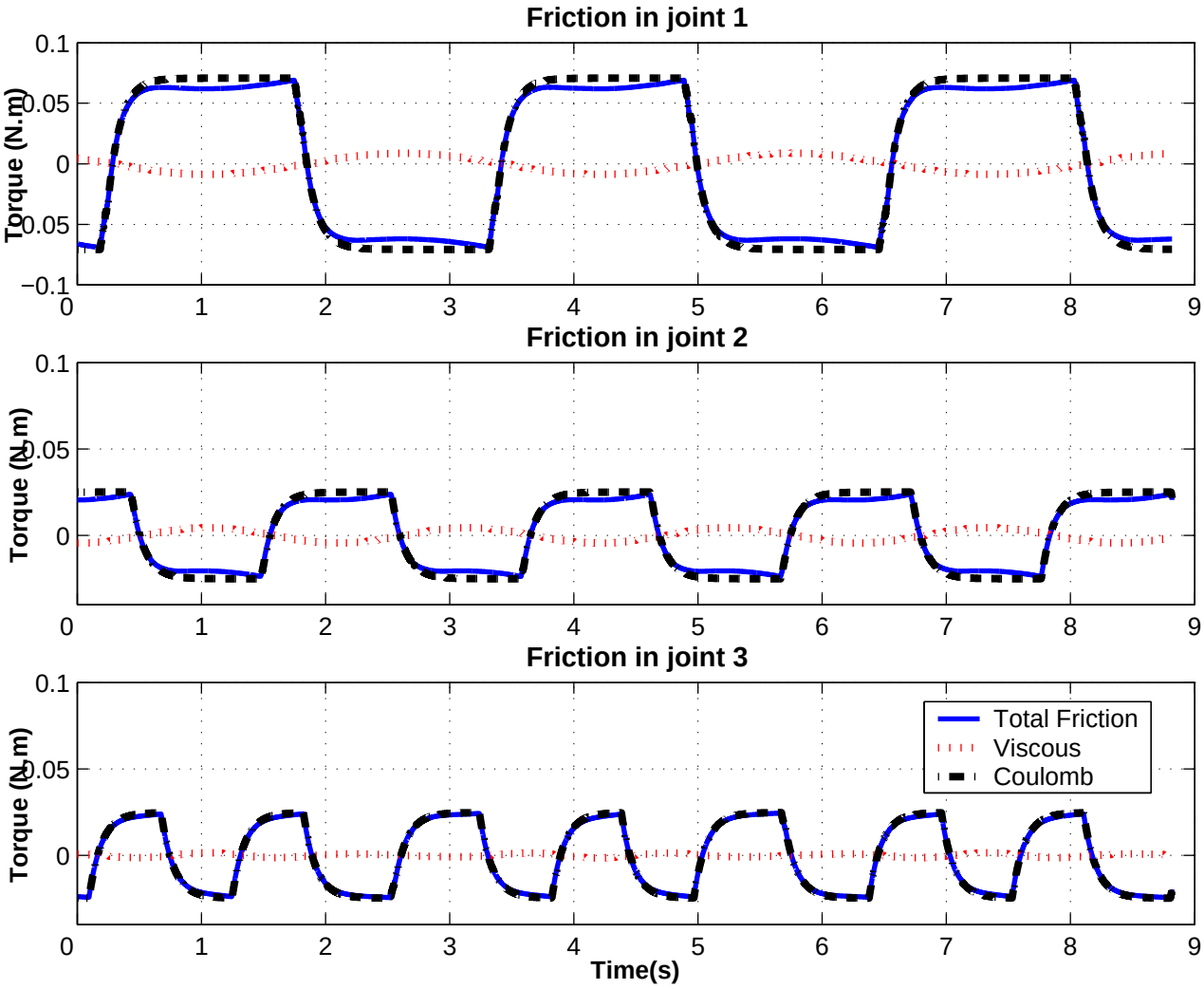
Friction in joint 1
Torque (N.m)
0.1
0.05
0
−0.05
−0.1
0
1
2
3
4
5
6
7
8
9
Friction in joint 2
Torque (N.m)
0.1
0.05
0
0
1
2
3
4
5
6
7
8
9
Friction in joint 3
Torque (N.m)
0.1
0.05
0
Total Friction
Viscous
Coulomb
0
1
2
3
4
5
6
7
8
9
Time(s)

Figure 9:

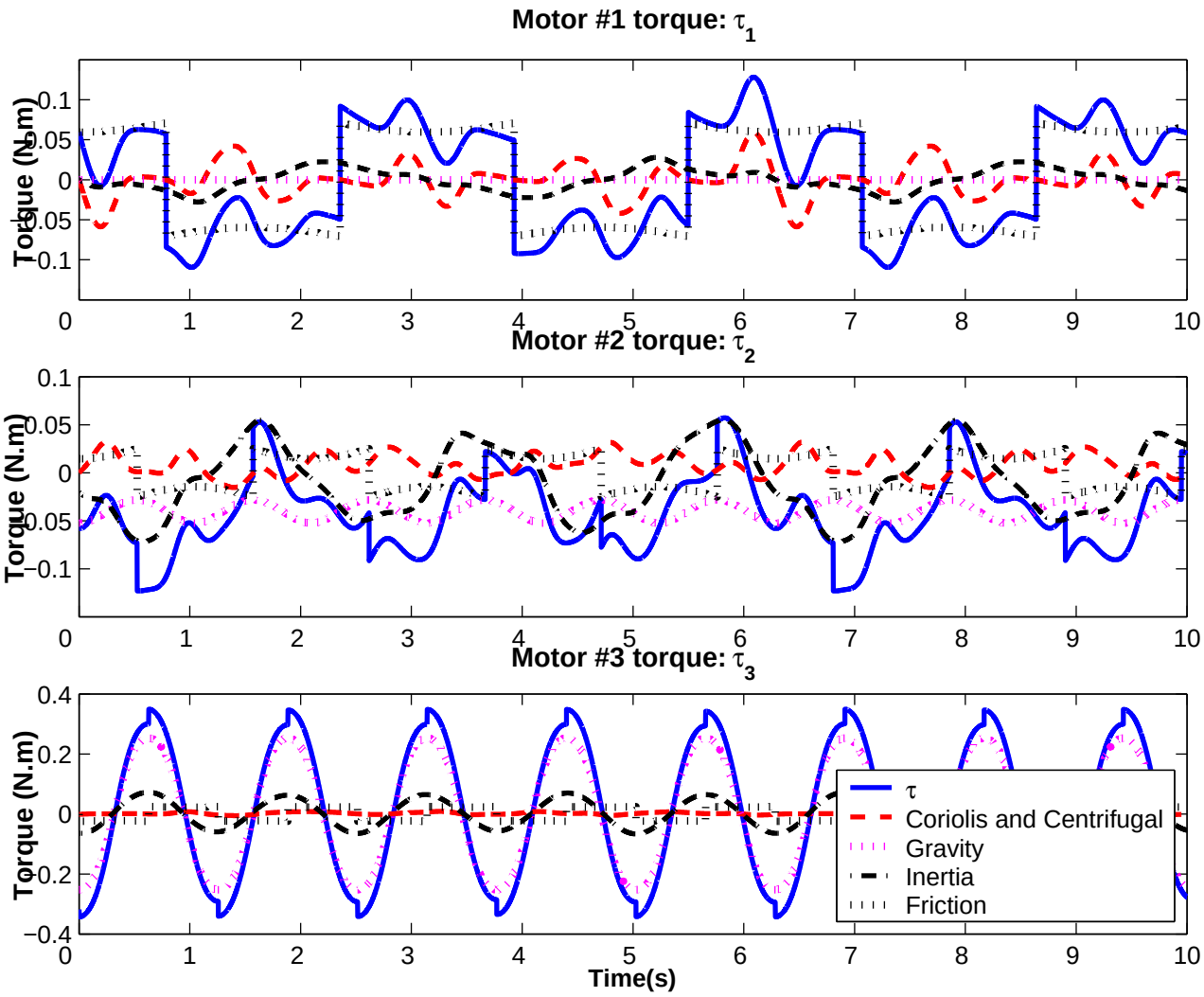
Motor #1 torque: τ1
Motor #2 torque: τ2
Motor #3 torque: τ3
Torque (N.m)
Time(s)
τ
Coriolis and Centrifugal
Gravity
Inertia
Friction

Figure 10:

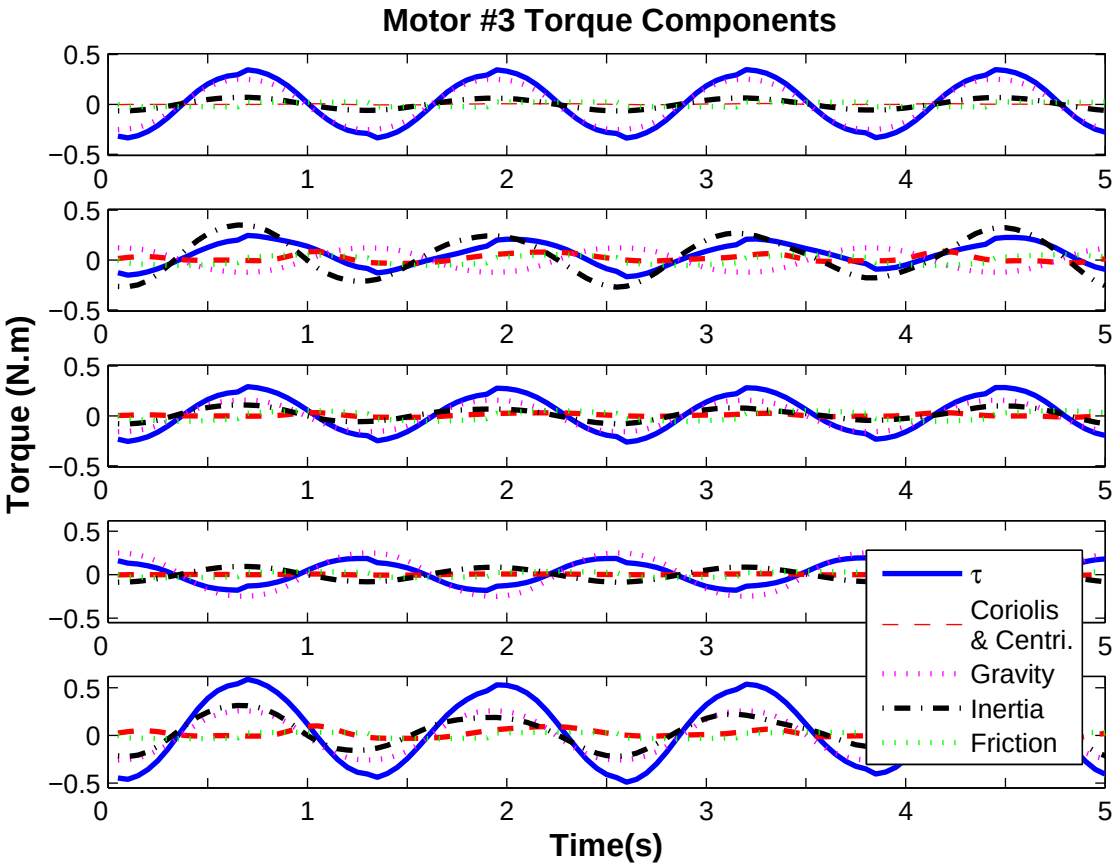
Motor #3 Torque Components
Torque (N.m)
Time(s)
τ
Coriolis & Centri.
Gravity
Inertia
Friction

Figure 11:

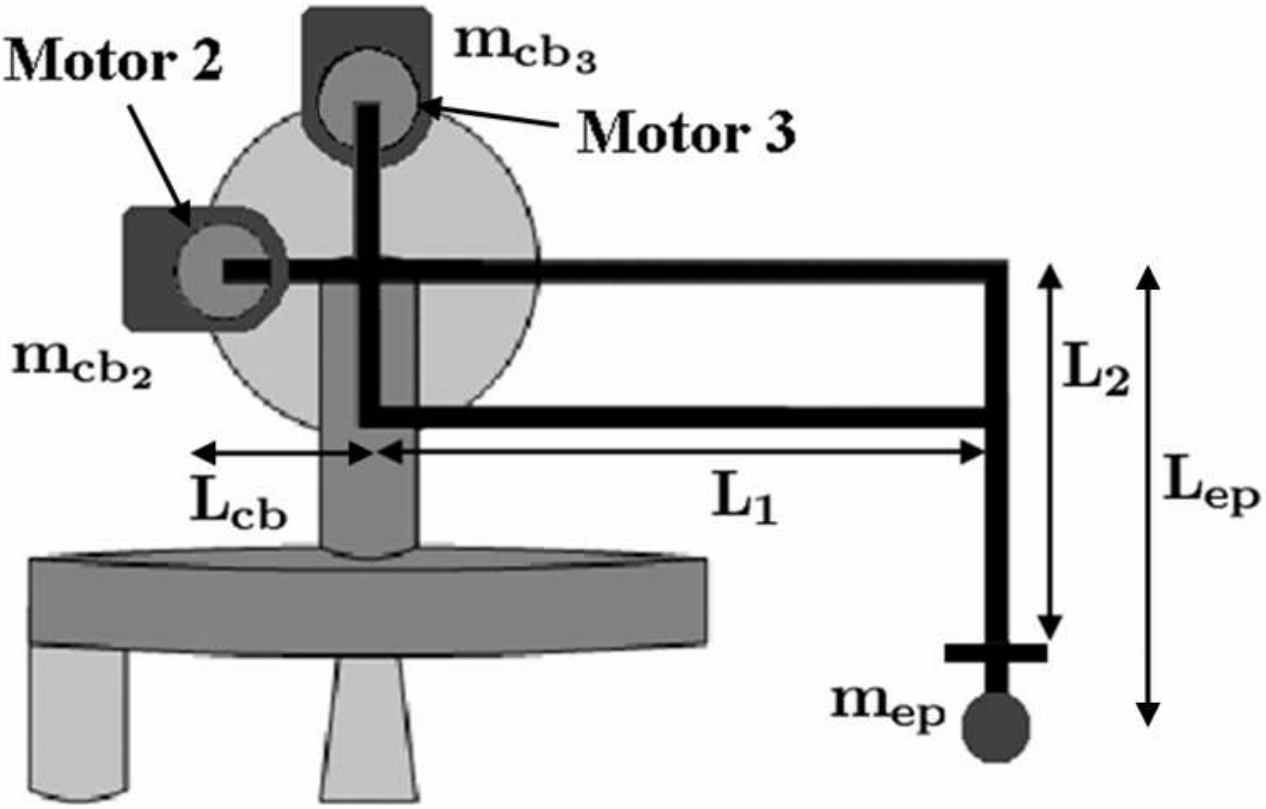

Figure 12:

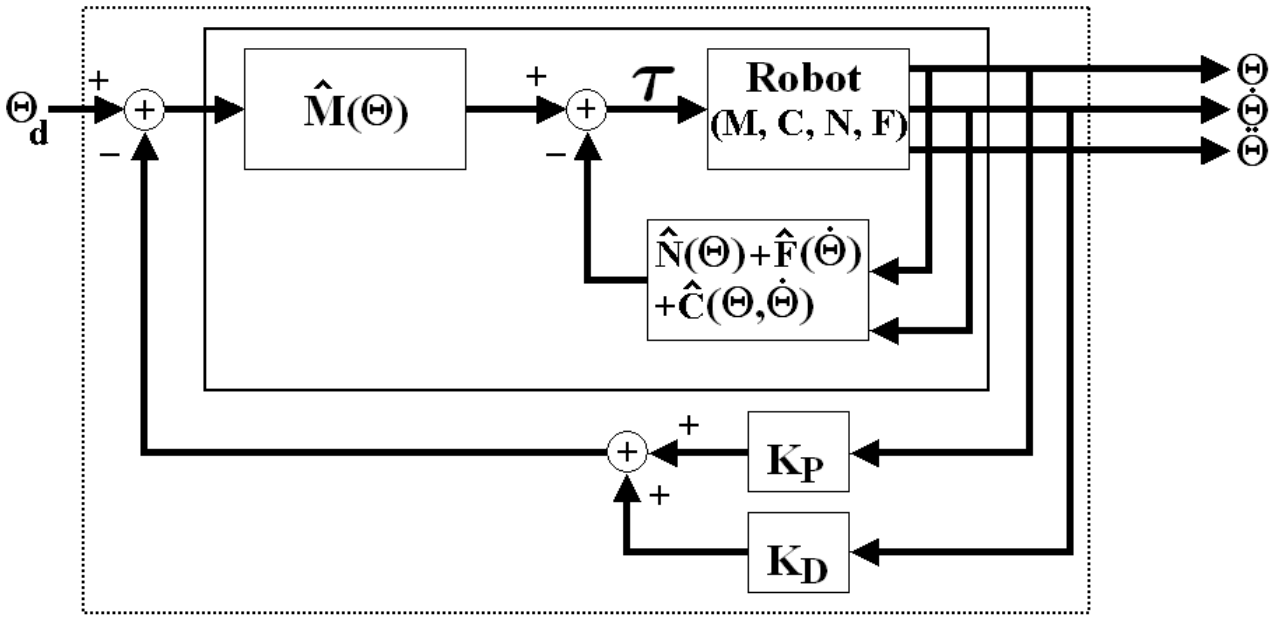

Figure 13:

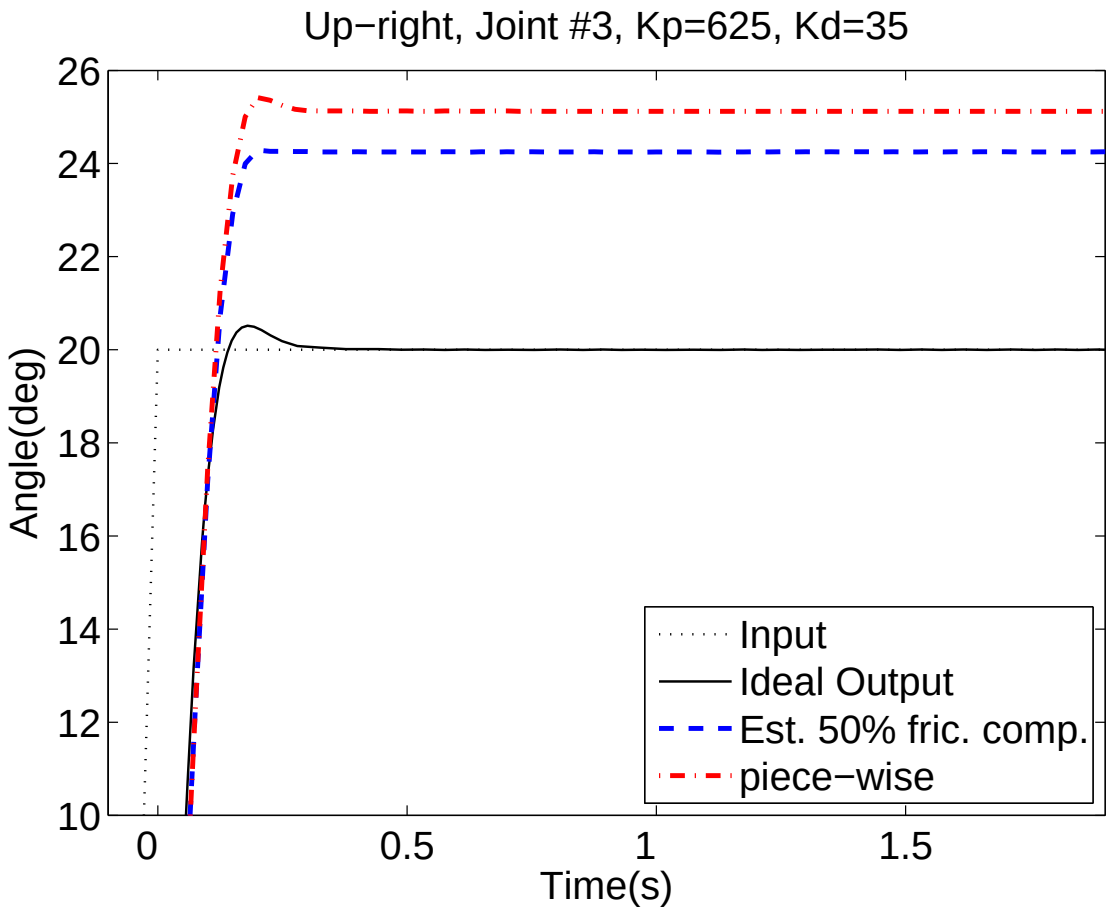
Up−right, Joint #3, Kp=625, Kd=35
26
24
22
20
18
16
14
12
10
Angle(deg)
0
0.5
1
1.5
Time(s)
Input
Ideal Output
Est. 50% fric. comp.
piece−wise

Figure 14:

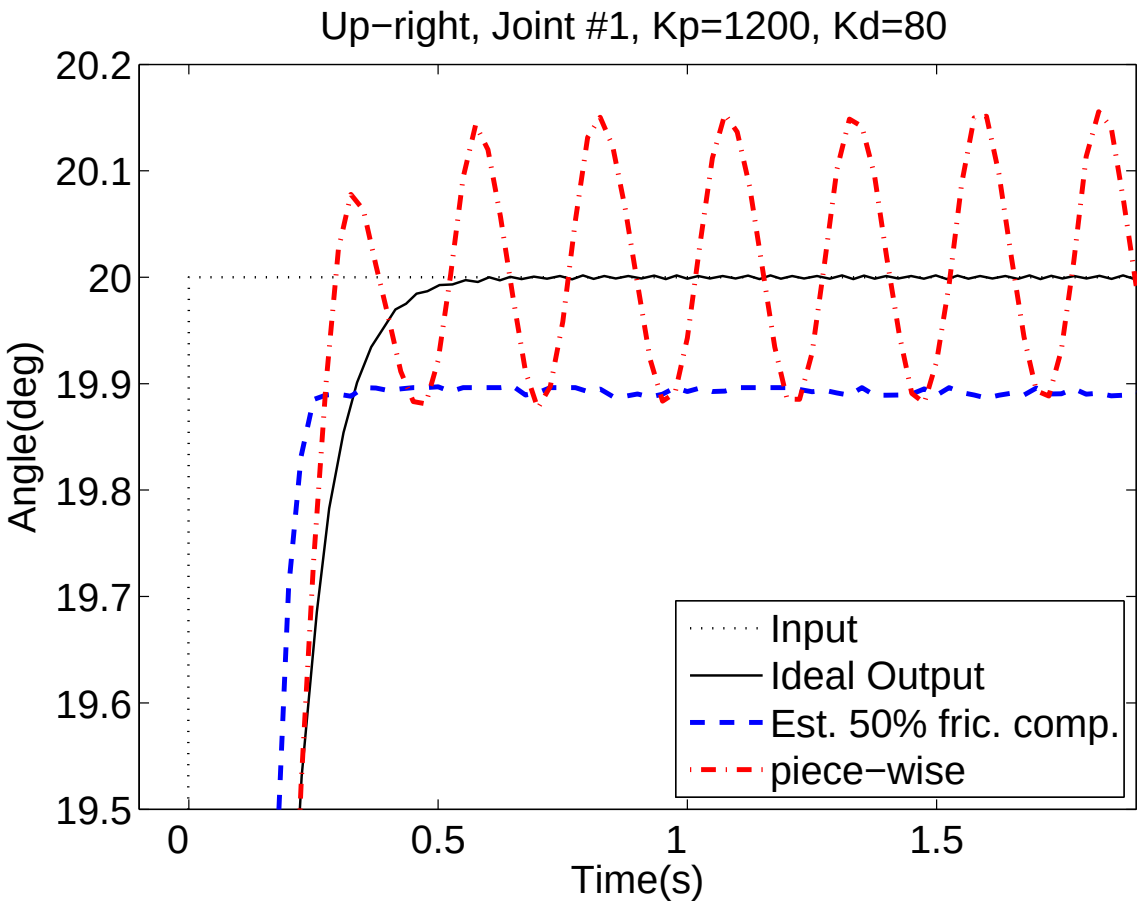
Up−right, Joint #1, Kp=1200, Kd=80
20.2
20.1
20
19.9
19.8
19.7
19.6
19.5
Angle(deg)
0
0.5
1
1.5
Time(s)
Input
Ideal Output
Est. 50% fric. comp.
piece−wise

Figure 15:

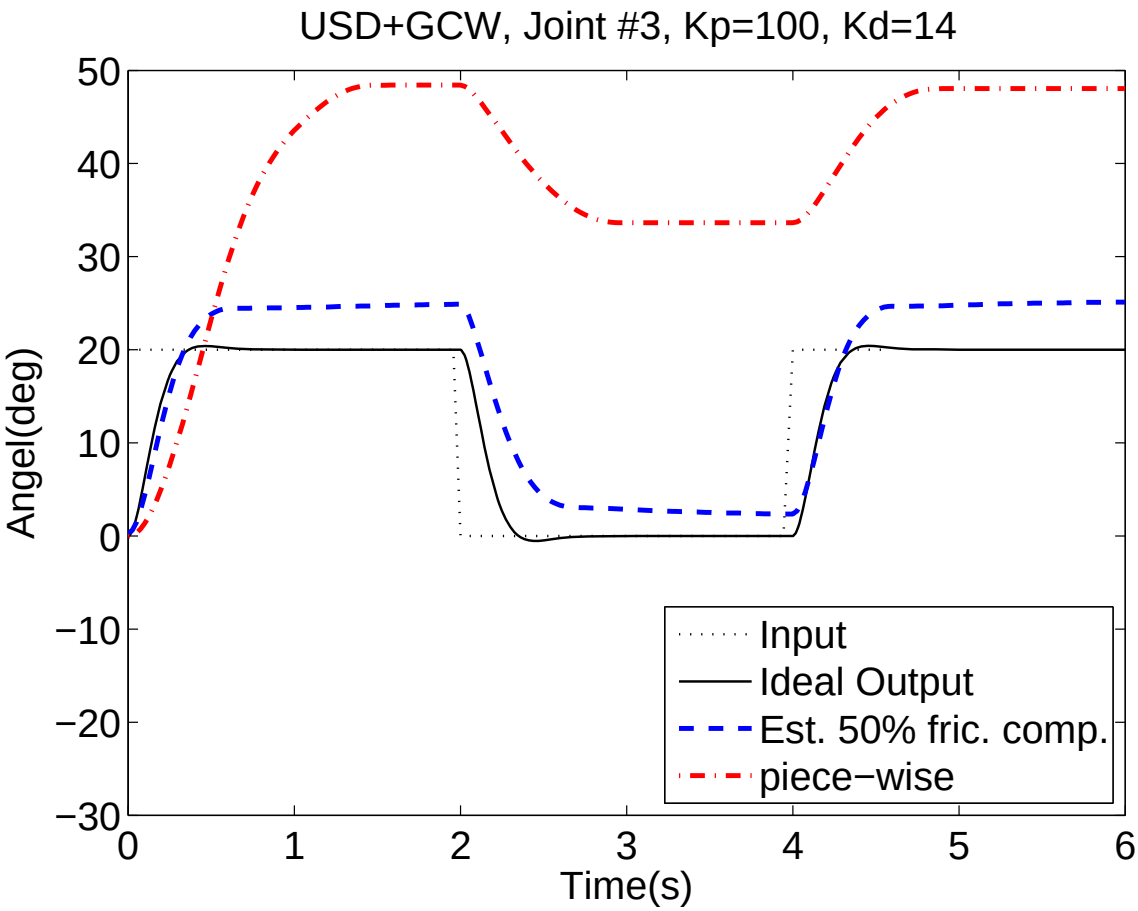
USD+GCW, Joint #3, Kp=100, Kd=14
Angel(deg)
Time(s)
50
40
30
20
10
0
−10
−20
−30
0
1
2
3
4
5
6
Input
Ideal Output
Est. 50% fric. comp.
piece−wise

Figure 16:

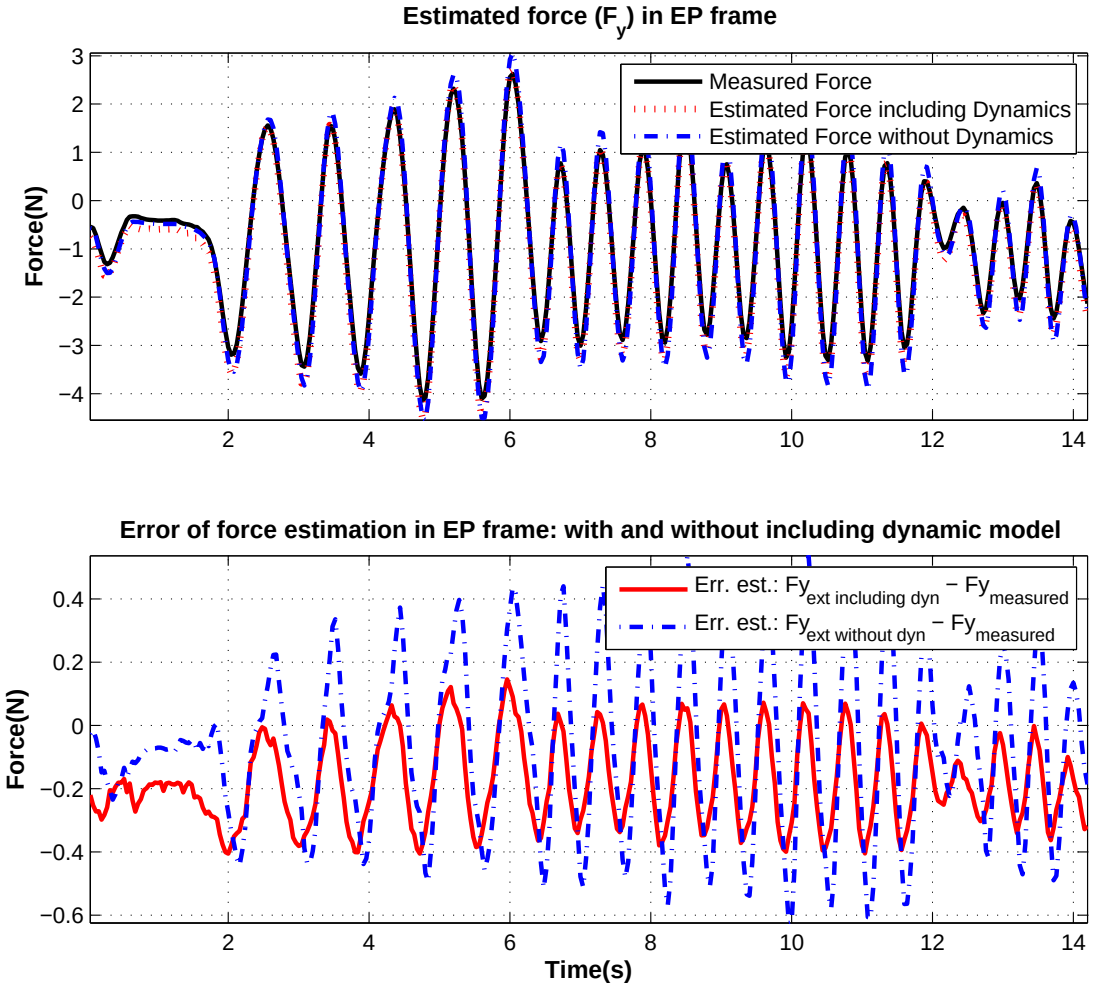
Estimated force (F_y) in EP frame
Measured Force
Estimated Force including Dynamics
Estimated Force without Dynamics
Force(N)
Error of force estimation in EP frame: with and without including dynamic model
Err. est.: $Fy_{ext\ including\ dyn} - Fy_{measured}$
Err. est.: $Fy_{ext\ without\ dyn} - Fy_{measured}$
Force(N)
Time(s)

Figure 17:

Figure Captions

Figure 1: Schematics of PHANTOM with its three motors, corresponding joint angles and the end-point Cartesian frame.

TWO-COLUMN

Figure 2: Passing the system dynamic equation through a low-pass filter.

ONE-COLUMN

Figure 3: PHANTOM Premium 1.5A in four different configurations: (a) Up-right, (b) using gimbal and counter-balance weight (GCW), (c) with force sensor mounted at the end-effector (FS), and (d) upside-down plus gimbal and counter-balance weight (USD+GCW).

TWO-COLUMN

Figure 4: Actual and estimated τ_L for the UR configuration; the solid black line shows the real filtered torque, the dotted line shows the predicted filtered torque using estimated π parameters (without friction in the dynamic model), and the dash-dot line shows the predicted filtered torque using the identified parameters from the piece-wise method.

ONE-COLUMN

Figure 5: Torque estimation error versus joint angular velocity for the UR configuration (without friction in the dynamic model).

ONE-COLUMN

Figure 6: Actual and estimated τ_L for the UR configuration using identified π parameters (with friction in the dynamic model).

ONE-COLUMN

Figure 7: Torque estimation error in filtered torque versus joint angular velocity for the UR configuration (with friction in the dynamic model).

ONE-COLUMN

Figure 8: Actual and estimated τ_L for the USD+GCW configuration using identified π parameters (with friction in the dynamic model).

ONE-COLUMN

Figure 9: Contribution of viscous and Coulomb friction terms in overall friction in all three joints for UR configuration.

ONE-COLUMN

Figure 10: Contribution of inertia, Coriolis and centrifugal, gravity, and friction in joint torque τ for UR configuration.

ONE-COLUMN

Figure 11: Contribution of inertia, Coriolis and centrifugal, gravity, and friction in the

joint 3 torque for UR, GCW, FS, USD, and USD+GCW configurations of the robot and its attachments (from top to bottom).

ONE-COLUMN

Figure 12: Schematics of the robot with End-Point attachment and counter-balance weights.

ONE-COLUMN

Figure 13: Block diagram of an inverse dynamics controller. The inverse dynamics inner loop and the PD outer loop are enclosed in solid and dashed boxes, respectively.

ONE-COLUMN

Figure 14: Inverse dynamics tracking output for joint 3 in UR configuration, with piece-wise method parameters from the piece-wise and the experimentally estimated parameters with 50% friction compensation, when $K_P = 625$ and $K_D = 35$.

ONE-COLUMN

Figure 15: Inverse dynamics tracking output for joint 3 in UR configuration, with piece-wise method parameters from the piece-wise and the experimentally estimated parameters with 50% friction compensation, when $K_P = 1200$ and $K_D = 80$.

ONE-COLUMN

Figure 16: Inverse dynamics tracking output for joint 3 in USD+GCW configuration, with the piece-wise method parameters from the piece-wise and the experimentally estimated parameters with 50% friction compensation, when $K_P = 100$ and $K_D = 14$.

ONE-COLUMN

Figure 17: Measured and estimated forces in the y-direction of the EP frame with and without inclusion of the system estimated dynamic model(top), and the corresponding force estimation errors (bottom).

ONE-COLUMN